Acta Pharmaceutica Sinica B 2026;16(8):5276−5296

Chinese Pharmaceutical Association
Institute of Materia Medica, Chinese Academy of Medical Sciences

Acta Pharmaceutica Sinica B

www.elsevier.com/locate/apsb
www.sciencedirect.com

ORIGINAL ARTICLE

Rhynchophylline rewires DLAT lipoylation *via* conformational control to reverse mitochondrial bioenergetic collapse against dopaminergic neuronal injury

Xiaomin Liang[a], Xunfang Yang[a], Shuhui Wang[a], Fangfang Zhuo[a], Xingzi Hou[a], Pengfei Tu[a], Yang Liu[c,*], Kewu Zeng[a,b,*], Qingying Zhang[a,*]

[a]*State Key Laboratory of Natural and Biomimetic Drugs and Department of Natural Medicines, School of Pharmaceutical Sciences, Peking University, Beijing 100191, China*
[b]*Department of Integration of Chinese and Western Medicine, School of Basic Medical Sciences, Peking University, Beijing 100191, China*
[c]*Center of Basic Medical Research, Institute of Medical Innovation and Research, Peking University Third Hospital, Peking University, Beijing 100191, China*

Received 10 May 2025; received in revised form 24 August 2025; accepted 19 October 2025

KEY WORDS

Rhynchophylline;
DLAT;
Lipoylation;
Mitochondrial dynamics;
Parkinson's disease;
Neuroprotection;
Target identification;
Thermal proteome profiling

Abstract Parkinson's disease (PD), the second most prevalent neurodegenerative disorder, is characterized by progressive loss of dopaminergic neurons in the substantia nigra. Although the molecular mechanisms of PD remain incompletely understood, mitochondrial dysfunction has emerged as a central pathological driver, highlighting the urgent need for therapies targeting mitochondrial homeostasis. In this study, we demonstrate that rhynchophylline (Rhy), a bioactive alkaloid from *Uncaria* species, exerts neuroprotective effects by restoring mitochondrial dynamics. Thermal proteome profiling identified dihydrolipoamide acetyltransferase (DLAT) as a direct target of Rhy. Genetic ablation of DLAT induced mitochondrial fragmentation and abolished Rhy-mediated beneficial effects on mitochondrial structure and function. Mechanically, Rhy binds to the N-terminal lipoyl domain of DLAT, allosterically disrupting its interaction with sirtuin 4 (SIRT4) and subsequently enhancing DLAT lipoylation, a critical post-translational modification for mitochondrial energy metabolism. *In vivo*, Rhy administration ameliorated motor deficits and dopaminergic neurodegeneration in both the 6-OHDA-induced and A53T α-synuclein transgenic PD mouse models. Single-nucleus RNA sequencing further highlighted the clinical relevance

*Corresponding authors.
E-mail addresses: qyzhang@bjmu.edu.cn (Qingying Zhang), ZKW@bjmu.edu.cn (Kewu Zeng), yliu_pu3h@bjmu.edu.cn (Yang Liu).

https://doi.org/10.1016/j.apsb.2026.06.016

of DLAT dysregulation in PD. Collectively, our findings establish Rhy as a promising PD therapeutic candidate and delineate DLAT as a pivotal node in therapeutic targets by promoting mitochondrial fusion and bioenergetics, offering a novel mechanistic avenue for neuroprotection.

1. Introduction

Parkinson's disease (PD), one of the most prevalent neurodegenerative disorders worldwide, is clinically characterized by progressive motor symptoms of bradykinesia, rigidity, resting tremor, and postural instability[1]. Neuropathologically, PD is defined by two hallmark features: the emergence of alpha-synuclein (α-syn) positive inclusion bodies, termed Lewy pathology, and degeneration of dopaminergic neurons in the substantia nigra (SN), accompanied by reduced dopamine (DA) levels[2]. The pathogenesis of PD is driven by multiple interconnected mechanisms, including neuroinflammation, oxidative stress, α-syn aggregation, mitochondrial dysfunction, ferroptosis, disrupted calcium homeostasis, and gut microbiota dysbiosis[3,4], of which mitochondrial dysfunction has been identified as a core factor in PD[5]. Mitochondria serve as critical regulators of cellular survival through ATP synthesis, calcium buffering, apoptotic signaling, and neurotransmitter recycling[6−8]. Given the exceptionally high bioenergetic demands of neurons, mitochondrial impairment is increasingly recognized as a common denominator in various neurological disorders[9−11]. Especially, mitochondria hold a distinctive position in PD for several other reasons. First, the current neurotoxin-induced models of PD rely on mitochondrial impairment to reproduce PD-like symptoms. Neurotoxins like 1-methyl-4-phenyl-1,2,3,6-tetrahydropyridine (MPTP)[12,13] and rotenone[14] trigger the death of dopaminergic neurons in humans and rats by directly inhibiting mitochondrial complex I activity[15]. Second, mutations in PD-associated genes (*PINK1*, *PARKIN*, *DJ-1*, and *LRRK2*) directly impair mitochondrial quality control pathways[16−18]. Third, clinical studies have identified various mitochondrial impairments in PD, including decreased mitochondrial numbers, imbalanced dynamics, decreased mitochondrial membrane potential (MMP), disrupted cristae structure, reduced respiratory capacity, and lowered ATP production[19]. Moreover, therapeutic approaches targeting mitochondrial proteins or inhibiting mitochondrial damage have been shown to alleviate neuropathological features in PD animal models and patient-derived cells[20,21], highlighting the potential of enhancing mitochondrial function as a promising treatment strategy for PD.

Mitochondria are organized in a highly dynamic tubular network that undergoes continuous remodeling through fusion and fission[22]. This dynamic process not only controls mitochondrial morphology but also regulates their function and subcellular distribution. Disruptions in either fusion or fission impair mitochondrial mobility, reduce energy production, and increase oxidative stress, ultimately leading to cellular dysfunction and death[23,24]. Mitochondrial fission is regulated by dynamin-1-related protein (DRP1)[25−27], where Ser 616 phosphorylation promotes the translocation of DRP1 from the cytosol to mitochondria, while Ser 637 phosphorylation reverses this process. The fusion process is governed by mitofusin-1/2 (MFN1/2) and optic atrophy 1 (OPA1)[28,29], which mediate outer and inner membrane fusion, respectively. Accumulating evidence from both toxin-induced and genetic models of PD supports the involvement of imbalanced mitochondrial dynamics and dysfunction in PD pathogenesis. Parkinsonian neurotoxins, such as 6-hydroxydopamine (6-OHDA), rotenone, and MPTP, have been shown to trigger mitochondrial fragmentation, culminating in the degeneration of dopaminergic neurons *in vitro*[30−32]. Fibroblasts derived from PD patients with *PINK1* or *PARKIN* mutations exhibit a more fragmented mitochondrial network[33−35]. These observations strengthen the role of imbalanced mitochondrial fusion and fission in PD pathogenesis and highlight the potential of targeting mitochondrial dynamics with small molecules as a therapeutic strategy to modulate disease progression.

Rhynchophylline (Rhy) is a plant-derived tetracyclic oxindole alkaloid isolated from *Uncaria* species. Experimental evidence indicates that Rhy exhibits blood−brain barrier permeability[36−38], laying a solid foundation for its neuroprotective properties. Multiple studies have elucidated a broad spectrum of neuropharmacological activities associated with Rhy, including anti-addiction, anticonvulsant, sedative, and anti-anxiety[39−41]. In particular, emerging studies have demonstrated the neuroprotective effects of Rhy in an MPTP-induced subacute PD mouse model[41,42], but the underlying molecular mechanism remains unclear. Recently, indole alkaloids have emerged as structural/functional classes of mitochondrial modulators[19], and we previously observed that the alkaloid fraction from *Uncaria rhynchophylla* (predominantly indole alkaloids) enhances mitochondrial fusion, prompting the present investigation into whether Rhy exerts protective effects on mitochondrial dynamics and the underlying mechanisms.

In this study, we demonstrate that Rhy restores mitochondrial dynamics and bioenergetics, with unbiased thermal proteome profiling (TPP) identifying DLAT as its key molecular target. Mechanically, Rhy enhances DLAT lipoylation by disrupting DLAT−SIRT4 interaction, which in turn promotes mitochondria fusion and function recovery. Therapeutically, Rhy administration ameliorated motor deficits and dopaminergic neurodegeneration in both the 6-OHDA-induced neurotoxin model and A53T α-syn transgenic PD mouse model. Taken together, these findings position Rhy as a promising PD therapeutic candidate and highlight DLAT as a critical node in regulating mitochondrial homeostasis.

2. Materials and methods

2.1. Chemicals and reagents

Rhynchophylline ($C_{22}H_{28}N_2O_4$; molecular weight 384.47) was obtained from Chengdu DeSiTe Biological Technology Co., Ltd (Chengdu, China) and confirmed by ^{1}H NMR and ^{13}C NMR data. HPLC analysis indicated a purity of >98%. 6-OHDA was

obtained from Sigma−Aldrich (St. Louis, USA). Fetal bovine serum (FBS) was from Animal Blood Ware (Woodstock, USA). High glucose Dulbecco's modified Eagle's medium (DMEM), phosphate buffer saline (PBS), opti-MEM, penicillin and streptomycin, and trypsin were purchased from Macgene (Beijing, China). Pronase was purchased from Roche Diagnostics GmbH (Mannheim, Germany). Bicinchoninic acid (BCA) protein quantitative kit, T4 polynucleotide kinase, and protease inhibitor cocktail were acquired from TransGen Biotech (Beijing, China). JC-1 staining kit, Mito-tracker Red CMXRos, and ATPLite™ kit were obtained from Beyotime (Shanghai, China). PKMito Orange (PKMO) was obtained from Genvivo (Nanjing, China). TMRE was from MedChemExpress (Monmouth Junction, USA). Solarbio (Beijing, China) provided the poly-L-lysine, Hoechst 33342 staining kit, *Escherichia coli* DH5α, and BL21 (DE3) strains. Bsmbl-v2 was purchased from New England Biolabs (Ipswich, USA). Thermo Scientific (Pleasanton, USA) supplied the chemiluminescent HRP substrate, protein labeling reagents, lipofectamine 2000, and lipofectamine RNAiMAX. PEI transfection reagent was from Servicebio (Wuhan, China). Santa Cruz Biotechnology (Dallas, USA), Abcam (Cambridge, UK), and Proteintech (Rosemont, USA) provided the primary and secondary antibodies. Merck Millipore (Burlington, USA) supplied the polyvinylidene difluoride (PVDF) membranes.

2.2. Cell lines and cell culture

The PC12 and HEK293T cell lines were sourced from the Cell Bank of Peking Union Medical College (Beijing, China). Human neuroblastoma SH-SY5Y cells were kindly provided by the Stem Cell Bank, Chinese Academy of Sciences (Shanghai, China). These cells were grown in high-glucose DMEM medium (supplemented with 10% FBS and a 1:100 penicillin/streptomycin antibiotic) and incubated at 37 °C in a 5% CO_2 environment.

2.3. Primary midbrain neuronal culture

Primary midbrain neurons were prepared from the ventral mesencephalon of embryonic Day 16 mouse embryos. Briefly, after extracting the whole brains from the embryos, the meninges and blood vessels were carefully removed. The midbrain tissue was isolated, minced with fine ophthalmic scissors, and enzymatically dissociated by incubating in a 0.2% trypsin solution (containing 0.1% glucose and 10 mmol/L HEPES) for 20 min at 37 °C. The digestion was terminated by adding an equal volume of DMEM supplemented with 10% FBS, 100 U/mL penicillin, and 100 μg/mL streptomycin. The tissue was then gently triturated into a single-cell suspension and plated onto culture plates or confocal dishes pre-coated with poly-L-lysine. After 4 h, the medium was replaced with Neurobasal medium supplemented with 2% B27 and 2 mmol/L L-glutamine. On Day 3, half of the medium was exchanged with fresh Neurobasal medium containing 5 μmol/L cytarabine to inhibit glial proliferation.

2.4. Mito-tracker staining assay

Cells were cultured in glass-bottom dishes and stained with 200 nmol/L Mito-tracker Red CMXRos at 37 °C for 30 min. Confocal imaging was conducted on a Leica SP8 microscope equipped with a 63× glycerol immersion lens, using excitation and emission wavelengths of 579 and 599 nm, respectively.

2.5. PKmito orange (PKMO) labeling of cells for imaging

PC12 and HEK293T cells were treated with DMEM containing 200 nmol/L PKMO for 30 min at 37 °C. After staining, the cells were rinsed three times with culture medium to clear unbound dye. Imaging was conducted on the Multimodality Structured Illumination Microscopy imaging system (NanoInsights-Tech., Ltd., Beijing, China) equipped with a 100× oil objective. Excitation of PKMO was achieved using a 561 nm laser. Images were then reconstructed using the SIM Imaging Analyser software (NanoInsights-Tech), including pre-processing and post-processing.

2.6. Mitochondrial membrane potential (MMP) assay

PC12 cells were cultured overnight in 24-well plates and then treated with 6-OHDA (150 μmol/L) and Rhy for 12 h. Next, MMP was measured following the manufacturer's instructions of the MMP assay kit with JC-1 or TMRE.

2.7. Transmission electron microscopy (TEM)

Transmission electron microscopy was performed by Wuhan Saiweier Biotechnology Co., Ltd. On cell and tissue samples. Samples were fixed in 3% glutaraldehyde and then post-fixed with 1% osmium tetroxide. Following dehydration in acetone, the samples were EPON 812-embedded. Semi-thin sections were stained with methylene blue, whereas ultrathin sections, prepared with a diamond knife, received uranyl acetate and lead citrate double staining. TEM images were acquired using a JEM-1400-FLASH transmission electron microscope.

2.8. Immunofluorescence assay

Cells were exposed to 6-OHDA and Rhy for 24 h, followed by PBS washing and fixation with 4% (*v*/*v*) formaldehyde at room temperature for 15 min. Samples were permeabilized with 0.1% Triton X-100 for 30 min, washed with PBST (PBS containing 0.2% Tween-20), and blocked with 2% BSA/PBST for 1 h at room temperature. Primary antibodies (rabbit anti-DLAT and mouse anti-SIRT4, Proteintech, cat. #66543-1-Ig and 13426-1-AP) diluted in 2% BSA/PBST, were applied at 4 °C overnight. After PBST washing, secondary antibodies (goat anti-rabbit/mouse) were applied. Cells were stained with 1 μg/mL DAPI in PBST for 15 min and stored in PBST until imaging. Fluorescence images were captured by a 63× glycerol immersion objective on a Leica SP8 confocal system. ImageJ (ver. 1.8) software was utilized to analyze fluorescence intensity and colocalization.

2.9. Measurement of ATP levels

The ATPLite™ kit was utilized to quantify ATP levels, normalized to the total protein content per microgram. A standard ATP curve was generated to determine ATP concentrations in cell lysates.

2.10. UHPLC−HRMS-based metabolomics and isotope tracing metabolic flux analysis

PC12 cells were divided into four groups: ^{12}C control group, ^{13}C control group, ^{13}C 6-OHDA-induced mitochondrial impairment model, and ^{13}C Rhy with 6-OHDA intervention. Following 24 h

incubation, all groups except for the ^{12}C control were transitioned to isotope-labeling medium containing glucose-free DMEM with 10 mmol/L [^{13}C 6]-glucose. After a 6 h metabolic labeling period, cellular samples were collected for subsequent UHPLC−HRMS-based metabolomic profiling and isotopic metabolic flux assessment. In short, after adding four volumes of cooled methanol: acetonitrile water (40:40:20, *v*/*v*/*v*) solution, cells were lysed *via* ultrasonication and vortexed for 1 min. After centrifugation at 13,000 × *g* for 30 min at 4 °C, the supernatant was dried and reconstituted in 100 μL of an 80:20 (*v*/*v*) acetonitrile-water solution. A second centrifugation step (13,000 × *g*, 30 min, 4 °C) was performed, and 60 μL of the resulting solution was loaded into auto-sampler vials for metabolomics and isotope tracing metabolic flux analysis using UHPLC−HRMS.

2.11. Target identification of Rhy by TPP approach

SN tissues from 6-OHDA-induced PD mice were lysed in PBS (pH 7.4) containing 1% EDTA-free cocktail and then centrifuged at 13,000 × *g* for 20 min at 4 °C to obtain the soluble proteins. The supernatant was divided into two aliquots; one was treated with 10 μmol/L Rhy (dissolved in DMSO) and the other with an equivalent volume of DMSO as a control. After incubation of the proteins with Rhy or DMSO for 2 h at 4 °C on a rotator at 10 rpm, each mixture was divided into three aliquots of 50 μL. The replications from both the vehicle and Rhy-treated groups were heated at 58 °C for 3 min and then cooled to room temperature. The heated lysates were centrifuged at 13,000 × *g* for 30 min at 4 °C to separate soluble proteins from aggregates. The supernatants were collected for quantitative proteomics analysis.

2.12. Drug affinity responsive target stability (DARTS) analysis

The SN lysate was treated with Rhy (1, 2, 5 μmol/L) at room temperature for 1 h. Subsequently, pronase with a concentration of 5 μg/mL was introduced and allowed to react for 15 min. Reactions were terminated by adding loading buffer, and the level of target proteins was analyzed by Western blotting.

2.13. Cellular thermal shift assay (CETSA) analysis

The SN lysate was divided into two aliquots, and cell lysates were treated with or without Rhy (10 μmol/L) for 2 h, and heated separately at the indicated temperature (46−67 °C) for 3 min. Supernatants were analyzed by Western blotting.

2.14. Immunoprecipitation (IP) assay

HEK293T cells were transfected with HA-DLAT for 48 h and treated with or without Rhy. Cellular lysates were subsequently immunoprecipitated by HA-tag antibody-bound magnetic beads at 4 °C for 6 h. The beads underwent centrifugation and were subjected to five washing cycles with IP buffer supplemented with 0.01% Triton X-100. Following this, the proteins obtained through immunoprecipitation were detected by immunoblotting.

2.15. Protein expression and purification

The N-terminal His-tag construct of DLAT, truncations, and mutants were overexpressed in *Escherichia coli* BL21 (DE3) cells and purified using affinity chromatography. In brief, cells were grown in LB medium (10 g/L peptone, 10 g/L NaCl, and 5 g/L yeast extract) at 37 °C to an optical density (OD_{600}) of 0.6. Subsequently, the temperature was cooled to 16 °C, and protein expression was initiated by adding 500 μmol/L IPTG, followed by continuous incubation at 16 °C for approximately 16 h. Cell pellets were harvested by 4000 × *g* centrifugation and lysed by sonication in 30 mL of lysis buffer (10 mmol/L imidazole, 20 mmol/L HEPES, 250 mmol/L NaCl). The lysates were centrifuged at 12,000 × *g* to remove insoluble components. The soluble fraction containing the target proteins was subsequently applied to a Ni-NTA affinity column for purification. The purification process involved sequential washing steps: first with 100 mL of lysis buffer (10 mmol/L imidazole, 20 mmol/L HEPES, 250 mmol/L NaCl), followed by 100 mL of wash buffer with increased imidazole concentration (50 mmol/L imidazole, 20 mmol/L HEPES, 250 mmol/L NaCl) to remove the nonspecifically bound proteins. Finally, the target proteins were eluted using a high-imidazole buffer (250 mmol/L imidazole, 20 mmol/L HEPES, 250 mmol/L NaCl). The purified protein fractions were concentrated to approximately 10 mg/mL by centrifugal filtration devices (Millipore, MA, USA) and stored at −80 °C for long-term storage.

2.16. DLAT knockout by CRISPR/Cas9

The DLAT knockout cell line was generated using the CRISPR-Cas9 system following standard protocols. Guide RNA sequences (sgRNAs) targeting DLAT were designed using CRISPOR (http://crispor.tefor.net/). The lentiviral vector lentiCRISPRv2 was linearized using Bsmbl-v2 restriction enzyme, synthesized oligonucleotides encoding either a non-targeting control or DLAT-specific sgRNAs were inserted using T4 polynucleotide kinase. Correct integration of the guide sequences was confirmed by Sanger sequencing.

For lentivirus production, HEK293T cells were transfected with the sgRNA-laden lentiCRISPRv2 vector along with the packaging plasmids psPAX2 and pMD2. G, using PEI as the transfection reagent. After 48 h of treatment, the viral supernatant was collected, filtered (0.45 μm), and used to transduce PC12 cells in the presence of polybrene (10 μg/mL) to improve transduction efficiency. Following 24 h of incubation, the medium was replaced with fresh culture medium, and cells were cultured for an additional 48 h. To select for positively transduced cells, the medium was replaced with zeocin-containing selection medium. Post-selection, cells were harvested and analyzed by Western blotting to verify DLAT knockout.

sgRNAs targeting DLAT (sequence from 5′ to 3′).

Lenti-CRISPRv2: DLAT-forward: GCCGCAGTTCGTTGCG GCAG.

Lenti-CRISPRv2: DLAT-reverse: CTGCCGCAACGAACTG CGGC.

2.17. DLAT knockdown with shDLAT lentivirus

The lentivirus containing shDLAT was constructed by Hanbio Biotechnology Co., Ltd (Shanghai, China). For transduction, the lentivirus was introduced into 293 T and SH-SY5Y cells in the presence of polybrene (10 μg/mL) for 24 h. Subsequently, stable DLAT-knockdown cells were generated through puromycin selection (2 μg/mL).

DLAT shRNA.

Forward: GATCCGGACCAGATGGTAGAATCACTCGAGT-GATTCTACCATCTGGTCCTTTTTTG.

Reverse: AATTCAAAAAAGGACCAGATGGTAGAATC-ACTCGAGTGATTCTACCATCTGGTCCG.

2.18. SIRT4 knockdown and overexpression cell lines

The SIRT4 knockdown cell line was generated using the CRISPR-Cas9 system. SgRNAs targeting SIRT4 were designed using CRISPOR (http://crispor.tefor.net/). For SIRT4 overexpression, the SIRT4 coding sequence was PCR-amplified and cloned into the pCDH-CMV-MCS-EF1-Puro lentiviral vector. Lentivirus was produced by co-transfecting HEK293T cells with the pCDH-SIRT4 plasmid, along with packaging plasmids (psPAX2, pMD2. G) using PEI transfection reagent. Viral supernatant was collected at 48 and 72 h post-transfection, filtered (0.45 μm), and used to transduce HEK293 cells in the presence of polybrene (8 μg/mL).

sgRNAs targeting SIRT4 (sequence from 5′ to 3′).

Lenti-CRISPRv2: SIRT4-foward: GTCTGGTATCCCCGAT TCGG.

Lenti-CRISPRv2: SIRT4-reverse: CCGAATCGGGGATAC CAGAC.

2.19. Western blotting analysis

Tissues or cells were lysed in RIPA buffer containing protease and phosphatase inhibitor cocktails. After centrifugation (13,000 × *g*, 20 min, 4 °C), the supernatants were collected, and protein concentration was quantified using a BCA assay kit. Proteins were denatured in loading buffer at 98 °C for 10 min, then resolved on 8%−12% SDS-PAGE gels and transferred to PVDF membranes. Membrane were blocked with 5% non-fat milk in TBST (1 h, room temperature), and then incubated with primary antibodies (overnight, 4 °C) against DLAT (Proteintech, 13426-1-AP); DRP1 (Biodragon, RM8248); p-DRP1^{Ser616} (Biodragon, BD-PP1318); p-DRP1^{Ser637} (Biodragon, BD-PP0841); OPA1 (MCE, HY-P80255); MFN2 (Biodragon, BD-PT2740); GAPDH (Proteintech, 60004-1-Ig); TH (Santa Cruz, sc-14007); Lipoic acid (Santa Cruz, sc-101354); VMAT2 (Santa Cruz, sc-390,285); HA (Solarbio, K200003M), SIRT2 (Abways, CY5865); SIRT4(Proteintech, 66543-1-Ig); LIAS (Proteintech, 11577-1-AP); AMPKα (Biodragon, RM1159); p-AMPKα (Biodragon, RM0088); p-STAT3 (Abmart, TC52210); p-EGFR (Abmart, PC1644); KIF5B (Abclonal, A20928); KIF5C(Biodragon, BD-PN3289); KIF1B (Biodragon, BD-PN4193). For secondary antibody incubation, anti-rabbit HRP (Proteintech, SA00001-2) and anti-mouse HRP (Proteintech, SA00001-1) were diluted in TBST. Protein bands were detected using enhanced chemiluminescence (ECL), and relative band intensities were quantified using ImageJ software (ver. 1.8).

2.20. Surface plasmon resonance (SPR) assay

The molecular interaction between Rhy and DLAT was analyzed by a Biacore 8 K system (GE Healthcare, Uppsala, Sweden). Through covalent immobilization *via* amine coupling chemistry, purified DLAT protein at a concentration of 50 μg/mL was fixed onto a CM5 sensor chip. Serial dilutions of Rhy ranging from 0.39 to 100 μmol/L, prepared in PBS supplemented with 5% DMSO, were introduced into the flow cell for binding analysis. The resulting interaction profiles were processed and quantified by Biacore evaluation software.

2.21. Microscale thermophoresis (MST) assay

Purified DLAT was first fluorescently labeled using commercial protein labeling reagents, and then Rhy (ranging from 0.03 to 100 μmol/L) was reacted with labeled DLAT in PBS buffer containing 0.01% Tween-20 at room temperature for 10 min. The reaction mixtures were then loaded into specialized glass capillaries and detected with the NanoTemper Monolith Instrument (NanoTemper Technologies, Munich, Germany). Thermophoretic movement of the protein-ligand complexes was monitored under controlled conditions. The results were further analyzed by MO. Affinity Analysis Software.

2.22. Molecular docking and dynamics simulations

The DLAT crystal structure (PDB: 2DNE) was retrieved from the RCSB PDB database, and the SIRT4 structure was obtained from AlphaFold. Protein−protein docking was performed using the HDOCK server, while ligand−protein docking employed the Schrödinger suite (2018) with the Induced Fit Docking protocol. Protein structures were prepared *via* the Protein Preparation Wizard, including bond order assignment, hydrogen addition, and water removal, followed by energy minimization (OPLS3 force field). A receptor grid was generated around the binding site, and docking was executed with Glide XP precision to sample flexible ligand/receptor conformations. Post-docking, 50-ns molecular dynamics simulations were conducted under NPT ensemble conditions using Berendsen thermostats.

2.23. Tryptophan fluorescence quenching assay

Recombinant DLAT protein was incubated with Rhy (0−200 μmol/L) in a quartz 96-well plate for 30 min. Tryptophan fluorescence emission spectra (310−450 nm) were recorded upon excitation at 280 nm (slit width: 1 nm) using a fluorescence spectrophotometer (PerkinElmer, Waltham, USA). The buffer background signal was subtracted from all measurements to obtain corrected fluorescence intensities.

2.24. Circular dichroism (CD) analysis

DLAT conformational changes induced by Rhy (0−500 μmol/L) were analyzed using a J-810 spectrophotometer (Jasco, Tokyo, Japan). Samples containing DLAT (40 μmol/L) with or without Rhy were loaded into a 1 mm path-length quartz cuvette, and CD spectra were recorded at 298 K. Spectra were acquired over 190−250 nm with a 0.1 nm data resolution, 50 nm/min scan rate, and three averaged scans per measurement. Background buffer contributions were subtracted for baseline correction.

2.25. Genetic and toxin-induced mouse models of PD

2.25.1. Establishment of 6-OHDA-induced PD mouse model

All experimental procedures were approved by the Ethical Institutional Animal Care and Use Committee of Peking University (Protocol LA2021217). Male C57BL/6 J mice (6 weeks old) were subjected to unilateral striatal lesions through stereotaxic injection of 6-OHDA. Following isoflurane-induced anesthesia, animals were secured in a stereotaxic frame (68,025, RWD, Shenzhen, China) and received precise microinjections of 2 μL 6-OHDA (4 μg/μL in 0.9% saline with 0.02% ascorbic acid) into the right striatum using coordinates referenced to Bregma: anteroposterior

+0.5 mm, mediolateral +2.0 mm, and dorsoventral −3.0 mm, with adjustments made according to the Paxinos and Watson mouse brain atlas. The neurotoxin was delivered at a constant rate of 0.4 μL/min using a microprocessor-controlled infusion system, with the injection cannula maintained *in situ* for an additional 10 min post-infusion to ensure proper diffusion and prevent backflow.

2.25.2. A53T transgenic mouse model

Male A53T transgenic mice (C57BL/6 J background) and wild-type (WT) littermates (7 months old) were obtained from Jackson Laboratory (Stock No. 004479). Initially, A53T mice were randomly divided into two groups: (1) vehicle-treated control and (2) Rhy-treated (10 mg/kg/day). An additional group of WT mice received vehicle alone as a baseline control. All mice were subjected to daily oral gavage administration of either Rhy or vehicle (equivalent volume) for six consecutive weeks.

2.26. Behavioral test

2.26.1. Grip strength test

Forelimb grip strength was assessed using a computerized YLS-13 A grip strength meter (Yiyan Scientific Research, Jinan, China). For the forelimb grip strength test, mice were allowed to grasp the sensor bar with their forepaws only, after which they were pulled horizontally by the tail until release. The peak force (g) was automatically recorded, with three consecutive trials performed per animal to ensure reliability.

2.26.2. Rotarod test

In the Rotarod test, the animals underwent adaptation training consisting of two sessions lasting 15 min each, separated by a 10-min rest period. After acclimatization, motor performance was assessed by measuring the duration of balance maintained on the rotating rod, with a maximum observation period of 180 s.

2.26.3. Apomorphine rotation test

Experimental mice were individually placed in a cylindrical chamber for 10 min to acclimate to the environment prior to the rotation test. Subsequently, apomorphine hydrochloride (0.5 mg/kg) was administered *via* intraperitoneal injection. The animals were then returned to the observation chambers for monitoring of rotational behavior. A total of 360° turns away from the lesioned side were manually counted over a 30-min observation period using a stopwatch.

2.26.4. Open-field test

Spontaneous locomotor activity was evaluated using an open-field test. The apparatus comprised a square arena measuring 40 cm × 40 cm × 40 cm. Each mouse was gently placed in the center of the arena and permitted to explore freely for 5 min. The movement of each mouse was captured by a video camera positioned centrally above the arena, and the recorded video data were subsequently analyzed using an automated video tracking system.

2.27. Pharmacokinetic analysis of Rhy

In the pharmacokinetic experiment, mice were randomly assigned to three dose groups receiving a single oral administration of Rhy (5, 10, or 20 mg/kg). Blood samples were collected 1 h post-dosing, corresponding to the approximate t_{max}. Immediately after blood collection, mice were transcardially perfused with 20 mL saline to eliminate residual intravascular blood. Brains were rapidly excised, weighed, and homogenized in ice-cold buffer. Tissue proteins were precipitated using a methanol: acetonitrile: water solution (4:4:2, *v*/*v*/*v*), followed by centrifugation (12,000×*g*, 15 min, 4 °C). The supernatant was vacuum-concentrated, and the dried residue was reconstituted in methanol for analysis.

2.28. In vivo biosafety and toxicological assessment

The potential *in vivo* toxicity was evaluated through serum biochemical profiling and histopathological examination. Blood samples were collected for quantification of hepatic (ALT, AST) and renal (urea, albumin) functional biomarkers, followed by necropsy in which major organs (liver, kidneys, heart, lungs, and spleen) were promptly excised, trimmed of connective tissue, and rinsed with cold PBS to remove residual blood; tissues were then fixed in 10% neutral-buffered formalin, processed through graded ethanol/xylene series, paraffin-embedded, sectioned at 5 μm, and stained with hematoxylin & eosin (H&E) for blinded histopathological evaluation of treatment-related alterations.

2.29. Single-nucleus RNA sequencing and bioinformatic analysis

Quality control filtering was performed to exclude low-quality nuclei and doublets using standard thresholds: nuclei with 200−5000 unique genes detected, <30,000 total UMIs, and ≤50% mitochondrial reads were retained. Filtered data were log-normalized, and highly variable genes were selected for downstream analysis. Dimensionality reduction was conducted *via* principal component analysis (PCA), followed by graph-based clustering (resolution = 0.5) on the top PCs to group transcriptionally similar nuclei. Clusters were visualized using Uniform Manifold Approximation and Projection (UMAP) and annotated based on canonical marker gene expression.

2.30. Statistical analysis

Data were presented as means ± standard deviation (SD). Statistical analyses were performed with GraphPad Prism (ver. 8.0, GraphPad Software, San Diego, USA). Differences between groups were analyzed by a two-tailed unpaired Student's *t*-test. Multiple group comparisons were evaluated through one-way analysis of variance (ANOVA). For statistical correlation, Pearson's correlation coefficient was used.

3. Results

3.1. Rhy ameliorates 6-OHDA-induced imbalanced mitochondrial dynamics

To determine whether Rhy protects against 6-OHDA-induced neurotoxicity by preserving mitochondrial health, we first assessed its effects on mitochondrial morphology. In primary midbrain neurons and PC12 cells, exposure to 6-OHDA induced profound mitochondrial fragmentation and collapse of the interconnected mitochondrial network. Notably, co-treatment with Rhy markedly mitigated these structural defects, preserving an elongated, tubular mitochondrial morphology (Fig. 1A−D). Ultrastructural analysis *via* PKMO imaging and TEM analysis further confirmed that Rhy

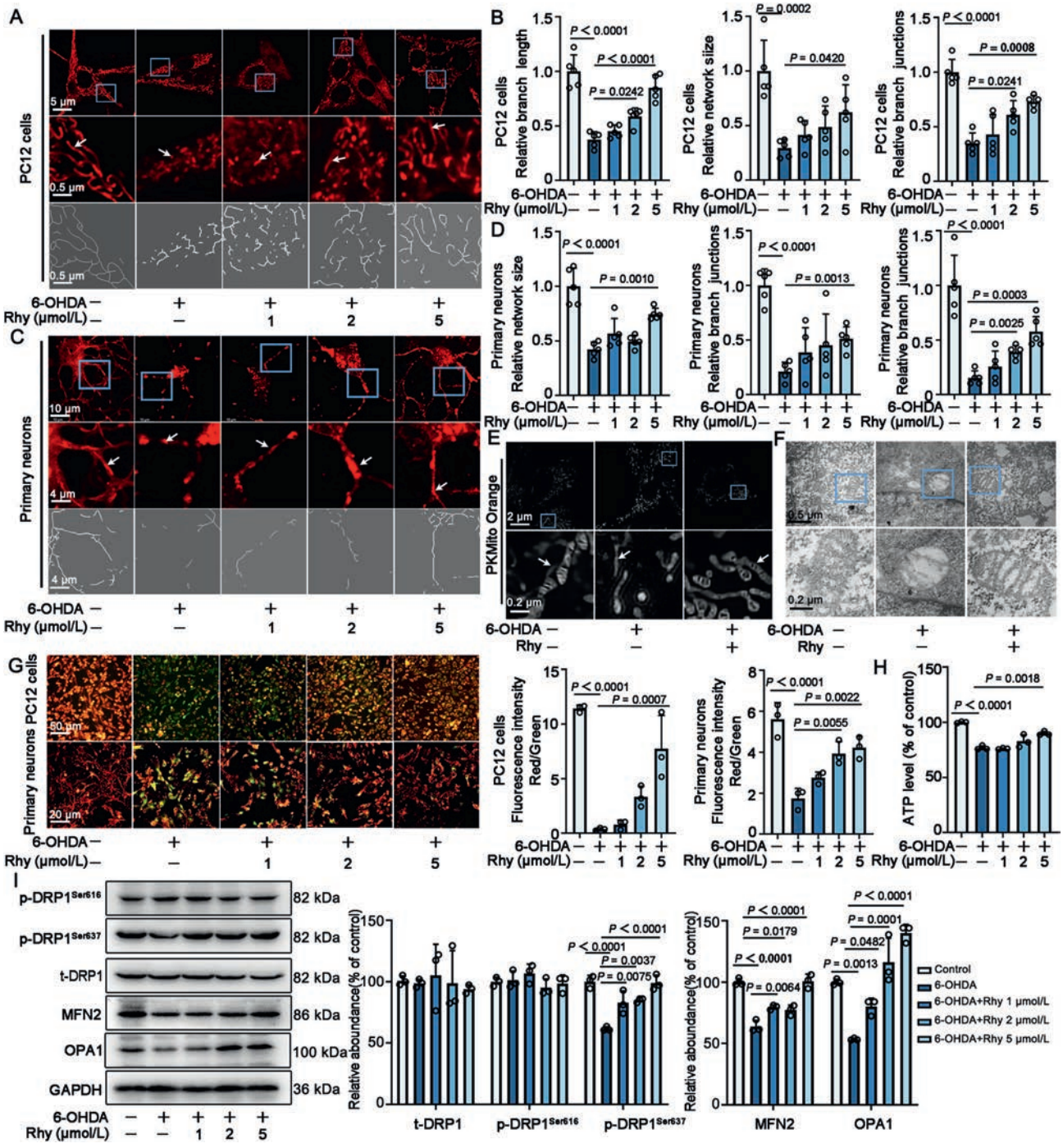

Figure 1 Rhy enhances mitochondrial function by promoting mitochondrial fusion. (A) Representative fluorescent images of mitochondria stained with Mito-tracker Red in PC12 cells. (B) Quantitative analysis of mitochondrial networks in PC12 cells using the MiNA plugin for ImageJ ($n = 5$ images). (C) Mitochondrial morphology in primary midbrain neurons visualized by Mito-tracker Red. (D) Mitochondrial network parameters quantified by MiNA analysis in primary midbrain neurons ($n = 5$ images). (E) High-resolution imaging of mitochondrial inner membranes using PKmito Orange (PKMO) microscopy. (F) Representative transmission electron microscopy (TEM) images of mitochondrial ultrastructure. (G) Mitochondrial membrane potential quantification by JC-1 ratio (Red/Green) in PC12 cells and primary midbrain neurons, $n = 3$ independent experiments. (H) Cellular ATP levels determined using ATPlite™ luminescence assay ($n = 3$). (I) Western blotting analysis of DRP1, p-DRP1^{Ser616}, p-DRP1^{Ser637}, MFN2 and OPA1 levels, following 6-OHDA (150 μmol/L) and Rhy treatment (1, 2, 5 μmol/L), $n = 3$ independent experiments. The data are presented as mean ± SD. Multiple group comparisons were evaluated through one-way analysis of variance (ANOVA). $P < 0.05$ was considered statistically significant.

maintained cristae morphology and membrane junction integrity (Fig. 1E and F). Transitioning to functional assessments, we observed that 6-OHDA triggered a dramatic collapse of mitochondrial membrane potential, a hallmark of mitochondrial dysfunction, which Rhy treatment effectively restored in both primary midbrain neurons and PC12 cells (Fig. 1G). Concurrently, Rhy prevented the 6-OHDA-induced depletion of intracellular ATP (Fig. 1H), confirming preservation of oxidative phosphorylation capacity. To mechanistically dissect Rhy-mediated protection, we examined proteins governing mitochondrial dynamics. Notably, Rhy upregulated key fusion mediators, including OPA1, p-DRP1^{Ser637}and MFN2, in 6-OHDA-exposed PC12 cells (Fig. 1I), strongly supporting a fusion-promoting mechanism underlying its neuroprotective effects. Taken together, these findings establish that Rhy counteracts 6-OHDA-induced mitochondrial dysfunction by shifting the balance toward fusion, preserving structural integrity, sustaining bioenergetic function, and ultimately promoting neuronal survival (Supporting Information Fig. S1).

3.2. DLAT serves as a direct target of Rhy in regulating mitochondrial fusion

To further elucidate the action targets of Rhy, we performed TPP and established a comprehensive workflow to screen Rhy-interacting proteins (Fig. 2A). Quantitative analysis identified 1380 proteins, among which 37 met our selection criteria ($|\log_2\text{-foldchange}| \geq 1$, $P \leq 0.05$) (Fig. 2B). Neuronal differential expression analysis revealed 8 promising candidates, with complexin-2 and dihydrolipoamide *S*-acetyltransferase (DLAT) emerging as top hits (Supporting Information Fig. S2). Considering the functional relevance of the top candidate proteins to mitochondrial biology[43,44], we prioritized DLAT, a well-characterized mitochondrial metabolic enzyme, for further investigation. (Fig. 2C).

Genetic validation using CRISPR-Cas9-generated DLAT knockout PC12 cells demonstrated that DLAT deletion significantly reduced OPA1 and p-DRP1^{Ser637} levels and abolished their Rhy-mediated upregulation (Fig. 2D). DLAT deficiency caused severe mitochondrial fragmentation with ultrastructural damage, including cristae loss (Fig. 2E−G, Supporting Information Fig. S3A), accompanied by membrane potential collapse that remained refractory to Rhy treatment (Fig. 2H and I). Notably, Rhy failed to rescue either the morphological defects or functional impairments in DLAT-deficient cells, suggesting DLAT mediates the neuroprotective effects of Rhy (Fig. S3B). These results collectively establish DLAT as an essential molecular target through which Rhy regulates mitochondrial fusion dynamics.

3.3. Rhy binds to the lipoyl domain of DLAT and enhances its lipoylation via allosteric inhibition of SIRT4 binding

Having identified DLAT as the principal mediator through which Rhy exerts its biological effects, we subsequently investigated whether this interaction occurs directly and delineated its underlying molecular mechanisms. SPR and MST revealed robust biophysical binding, yielding dissociation constants (K_D) of 2.7 and 1.6 μmol/L, respectively (Fig. 3A and B), confirming a specific interaction. Notably, Rhy binding enhanced DLAT stability, protecting it from proteolytic degradation (Fig. 3C and D) and thermal denaturation (Fig. 3E−G). Together, these findings establish DLAT as a direct target of Rhy, underscoring its role in mediating Rhy's neuroprotective effects in PD.

To elucidate the structural basis of Rhy−DLAT binding, we mapped the interaction domain within DLAT's three-domain architecture (Fig. 3H): the N-terminal lipoyl domain (L), central subunit-binding domain (B), and C-terminal inner domain (I). Given that the small, hinge-rich B domain is unlikely to accommodate small molecules, we tested truncated constructs (ΔL, ΔI) *via* SPR. Rhy bound ΔI (K_D = 2.0 μmol/L) but not ΔL (K_D = 59.4 μmol/L), localizing its binding site to the L domain (Fig. 3I−K). Molecular docking identified hydrogen bonding and hydrophobic interactions at this site (Fig. 3L). Mutating critical residues (P13A/G52A) weakened Rhy binding (K_D = 38.5/57.5 μmol/L; Fig. 3M, Supporting Information Fig. S4) and abolished Rhy's neuroprotection in DLAT-knockdown cells reconstituted with mutant versus wild-type DLAT (Fig. 3N), confirming the functional necessity of this interaction.

Lipoylation of conserved lysine residues in the L domain, a post-translational modification (PTM) essential for DLAT's acetyltransferase function, drives pyruvate dehydrogenase complex (PDC)-dependent acetyl-CoA generation (Fig. 4A). To investigate Rhy's regulatory role in DLAT lipoylation, we transfected HEK293T cells with HA-DLAT and performed immunoblot analysis. Remarkably, Rhy treatment significantly enhanced DLAT lipoylation without affecting total DLAT protein expression (Fig. 4B). Consistent with its effect on DLAT lipoylation, Rhy treatment dose-dependently enhanced PDC activity (Fig. 4C). This stimulation exerted a pronounced effect on the TCA cycle, as evidenced by metabolic tracing assays: compared to controls, the model group exhibited reduced enrichment of [$^{13}C_4$]-Suc [$^{13}C_4$]-Fum, and [$^{13}C_4$]-MA, key intermediates reflecting mitochondrial oxidative flux. Strikingly, Rhy reversed this decline (Fig. 4D and E), indicating restored oxidative metabolism. These findings underscore lipoylation's pivotal role in regulating cellular bioenergetics.

Among the established regulators of DLAT lipoylation (LIAS, SIRT2, SIRT4), our co-immunoprecipitation (Co-IP) assays revealed that Rhy specifically disrupts the interaction between DLAT and the mitochondrial deacylase SIRT4 (Fig. 4F). To functionally validate SIRT4 as the primary mediator of DLAT delipoylation, we established stable SIRT4-overexpression and knockdown cell lines. Strikingly, SIRT4 knockdown substantially enhanced DLAT lipoylation, whereas overexpressing SIRT4 caused a marked decrease (Fig. 4G). These findings not only definitively demonstrate SIRT4's delipoylase activity toward DLAT in our system but also corroborate previous investigations[45]. Crucially, Rhy treatment failed to enhance DLAT lipoylation in SIRT4 knockdown cells. Complementary confocal imaging showed that Rhy treatment reduced DLAT−SIRT4 spatial colocalization (Supporting Information Fig. S5A), reinforcing our model in which Rhy modulates DLAT lipoylation by disrupting DLAT−SIRT4 binding. To investigate its potential pathogenic relevance, we analyzed single-cell RNA sequencing data from postmortem midbrain tissues of PD patients versus controls, comparing expression levels of LIAS, SIRT2, and SIRT4. Strikingly, PD patients exhibited consistently higher SIRT4 expression compared to healthy individuals (Fig. S5B−S5D). Taken together, these results support our hypothesis that pathological SIRT4 upregulation drives excessive DLAT−SIRT4 interaction and delipoylation in PD. Importantly, Rhy appears to reverse this defect by preventing DLAT−SIRT4 binding, thereby restoring

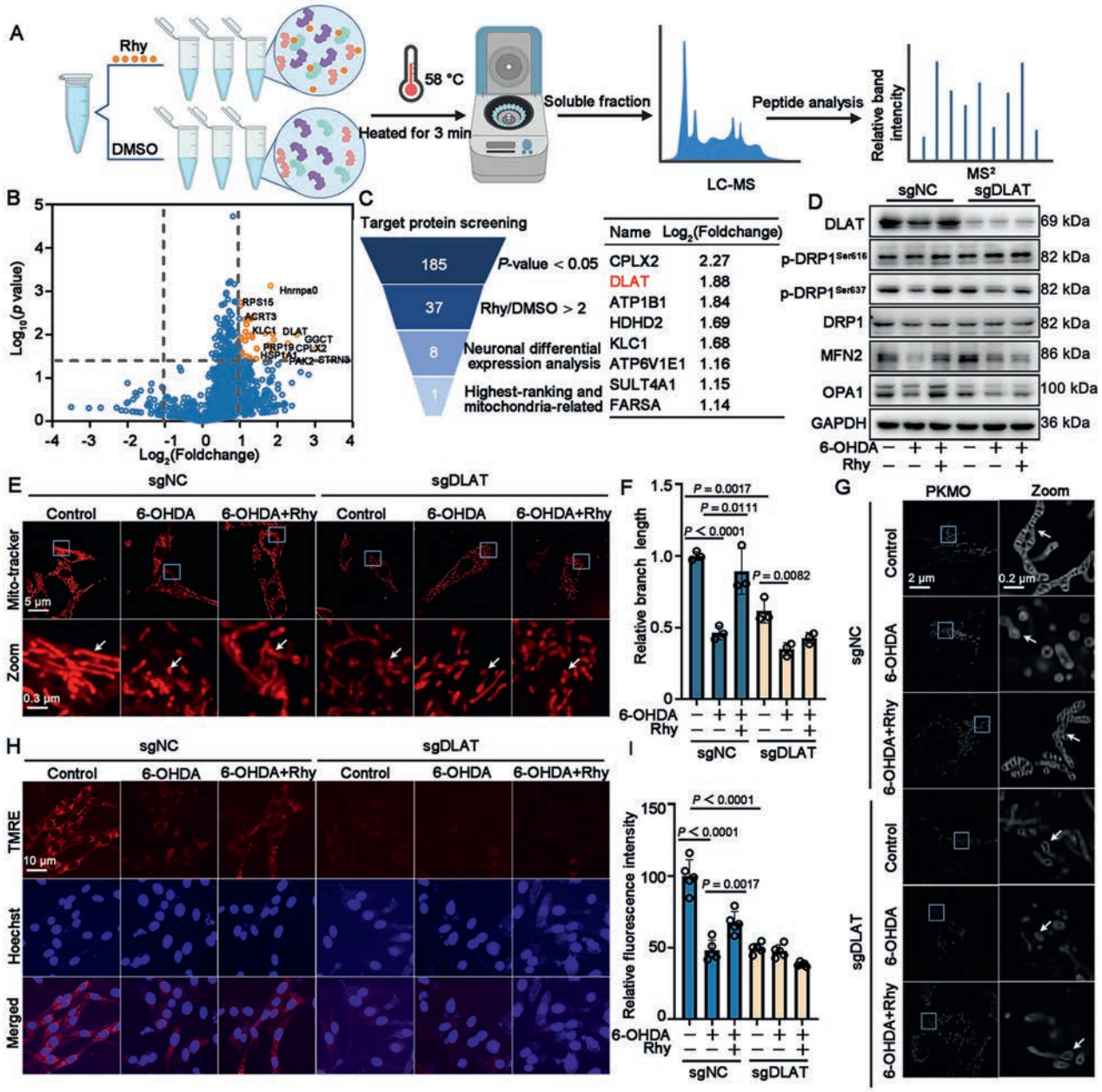

Figure 2 DLAT mediates Rhy-induced mitochondrial fusion regulation. (A) Experimental workflow for identifying potential targets of Rhy using thermal proteome profiling (TPP) strategy. (B) Volcano plot of TPP results and screening strategy for Rhy's anti-PD targets. (C) Schematic representation of the target screening and prioritization pipeline. (D) Western blotting analysis showing Rhy-regulated mitochondrial dynamics proteins (OPA1, p-DRP1^{Ser637}) in control *versus* DLAT-KO cells ($n = 3$). (E, F) Representative confocal images (E) and quantification (F) of mitochondrial networks visualized by Mito-tracker Red ($n = 3$ fields). (G) Super-resolution microscopy images of mitochondrial cristae structures labeled with PKmito Orange (PKMO), $n = 3$ images. (H, I) TMRE staining reveals mitochondrial membrane potential alterations ($n = 5$ fields). The data are presented as mean ± SD. Multiple group comparisons were evaluated through one-way analysis of variance (ANOVA). $P < 0.05$ was considered statistically significant.

DLAT lipoylation and ameliorating mitochondrial dysfunction in neuronal models.

Conformational changes in proteins can modulate binding affinities with interacting partners. Combining tryptophan fluorescence and circular dichroism spectroscopy, we demonstrated that Rhy induced structural rearrangements in DLAT. The observed quenching of tryptophan fluorescence suggested Rhy-mediated alterations in the local microenvironment of aromatic residues (Fig. 4H). Circular dichroism spectral analysis revealed distinct perturbations in DLAT's secondary structure, notably affecting β-sheet regions (evidenced by characteristic negative [218−220 nm] and positive peaks [195−198 nm]) and β-turn motifs (negative peak ∼200 nm; positive peak ∼205 nm), signatures associated with its lipoylation domain (Fig. 4I). These structural shifts

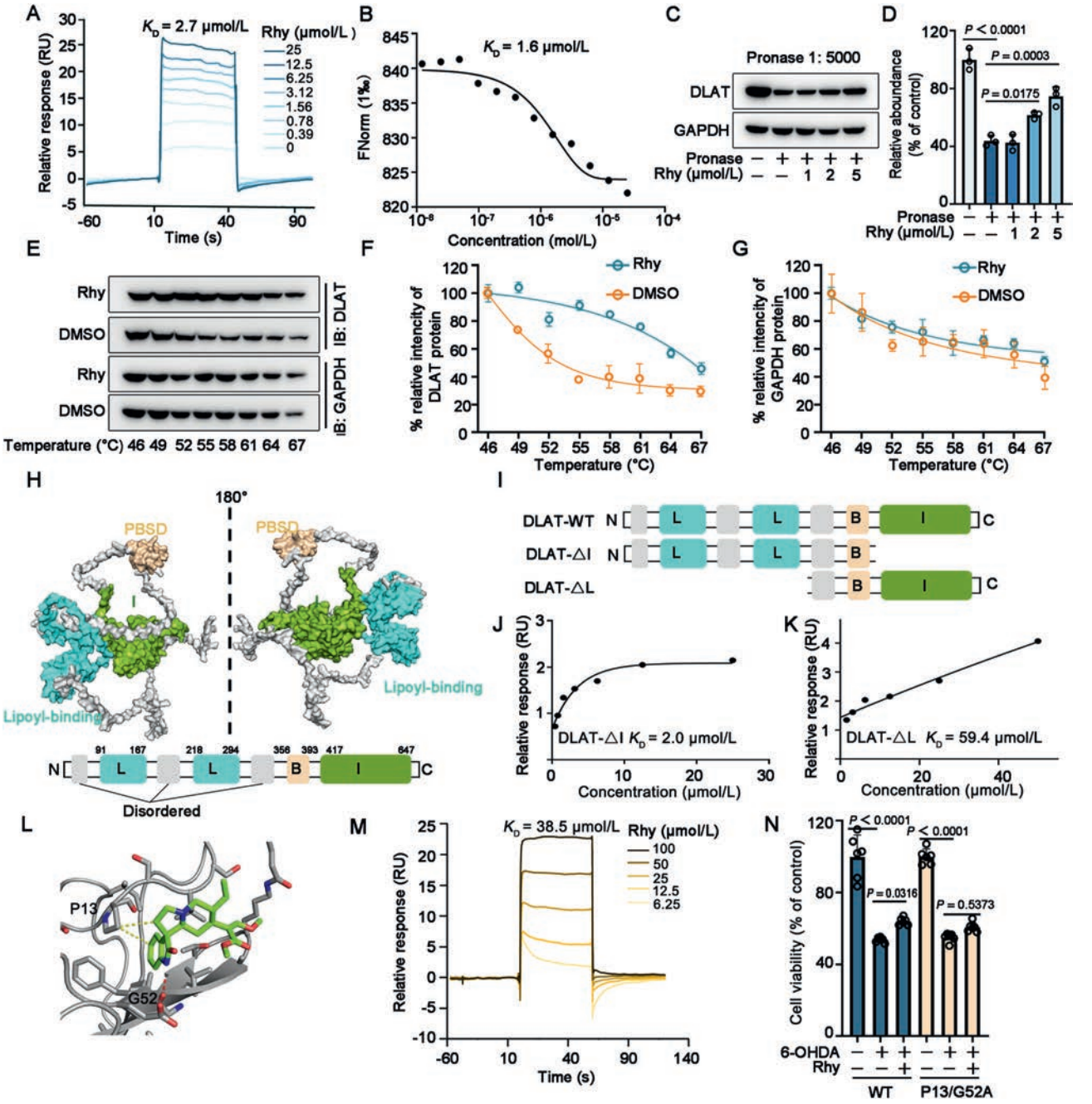

Figure 3 Rhy directly binds to the L domain of DLAT. (A) SPR analysis of binding affinity between Rhy and DLAT. (B) MST analysis of binding affinity between Rhy and DLAT. (C, D) DARTS assays confirmed Rhy−DLAT interaction. (E−G) CETSA revealed thermal stabilization of DLAT by Rhy; GAPDH served as the negative control ($n = 3$). (H) Schematic representation of DLAT domain architecture and tertiary structure. (I) Design strategy for two truncated DLAT constructs. (J, K) SPR assays evaluating Rhy binding to DLAT truncations. (L) Predicted binding mode of Rhy within the DLAT L domain, derived from molecular docking. (M) SPR analysis of Rhy binding to a site-directed DLAT mutant. (N) MTT-based assessment of neuroprotective activity by Rhy in SH-SY5Y cells with shDLAT knockdown, rescued by WT or mutant DLAT expression ($n = 6$). The data are presented as mean ± SD. Multiple group comparisons were evaluated through one-way analysis of variance (ANOVA). $P < 0.05$ was considered statistically significant.

correlated with SPR data confirming Rhy's specific binding to the L domain. Through molecular dynamics simulations, we observed Rhy-induced weakening of DLAT−SIRT4 binding, as evidenced by the elevation in free energy from −48.49 to −37.22 kcal/mol. Crucially, Rhy-induced deformation of DLAT's L domain sterically blocked the lipoylation branch from accessing SIRT4's catalytic H161 pocket, thereby impairing hydrolysis (Fig. 4J). Collectively, these results establish that Rhy remodels DLAT conformation to weaken SIRT4 binding while promoting lipoylation-dependent restoration of mitochondrial dynamics.

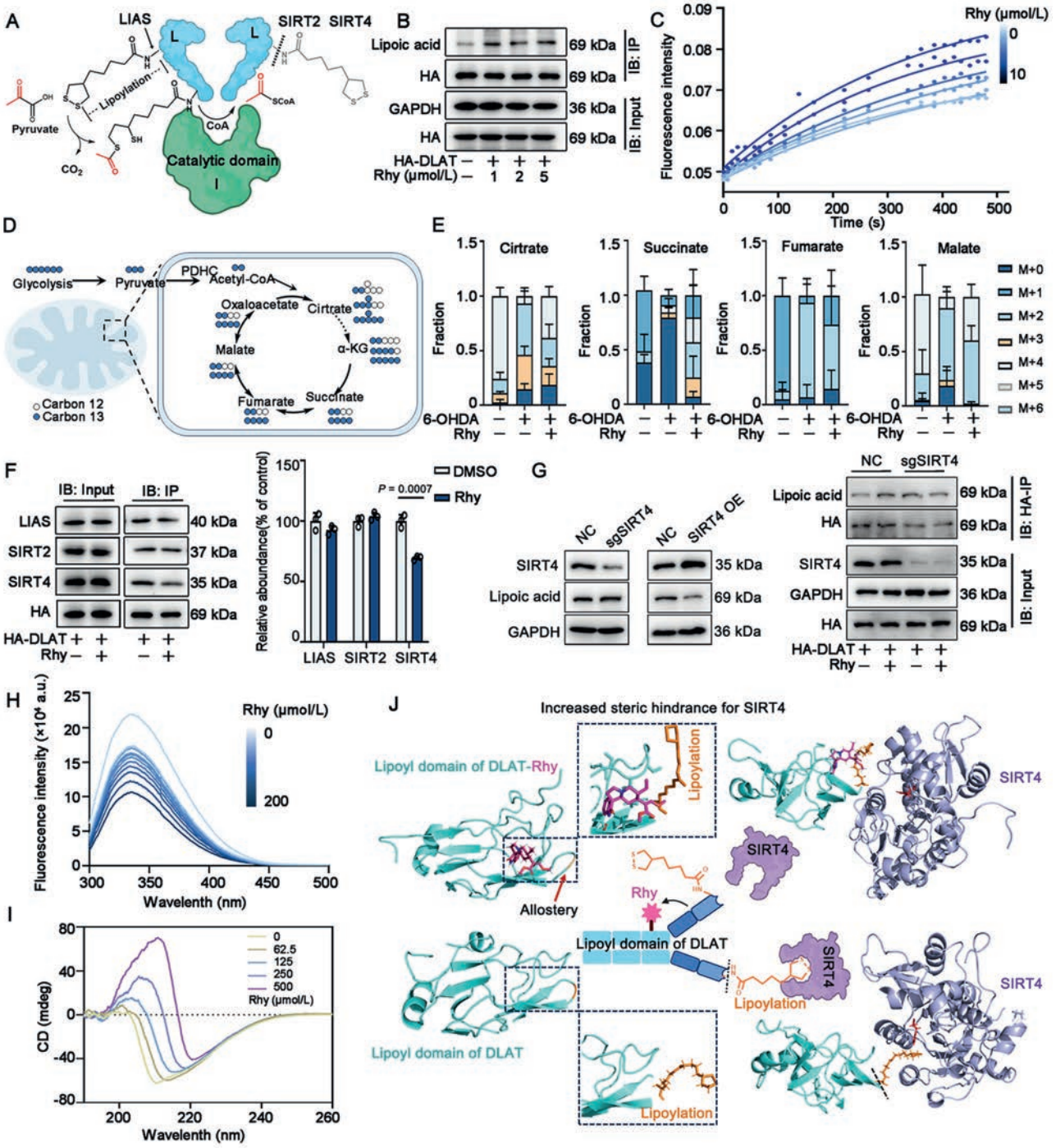

Figure 4 Rhy enhances DLAT lipoylation by disrupting DLAT−SIRT4 interaction. (A) Schematic depicting the enzymatic role of DLAT in PDC. As a key catalytic subunit, DLAT converts pyruvate to acetyl-CoA, bridging glycolysis and the TCA cycle. The L domain facilitated substrate channeling *via* a "swinging arm" mechanism to the interaction I domain for acetyl-CoA synthesis (Figure was created with Biorender.com). (B) Western blotting analysis of DLAT lipoylation levels following Rhy treatment. (C) PDC enzymatic activity assay in response to Rhy. (D, E) TCA cycle metabolic flux assessed using ^{13}C-labeled glucose. Isotopologue distributions (M+1 to M+6) denote the incorporation of 1−6 ^{13}C atoms, tracking carbon flow through metabolic intermediates. (F) Co-IP assays of DLAT−SIRT4 interaction. HEK293T cells expressing HA-tagged DLAT were treated with Rhy for 4 h, followed by IP with anti-HA antibody and Western blotting ($n = 3$). (G) Validation of SIRT4 as the primary regulator of DLAT delipoylation *via* gain and loss-of-function assays. Rhy-induced DLAT lipoylation depends on SIRT4 activity. (H) Tryptophan fluorescence spectroscopy revealing Rhy-induced conformational changes in DLAT. (I) CD spectra analysis of Rhy-mediated DLAT structural alterations. (J) Molecular dynamics simulations comparing DLAT−SIRT4 complex stability with or without Rhy, quantifying binding free energy shifts.

3.4. DLAT lipoylation maintains mitochondrial dynamic homeostasis

To determine whether DLAT lipoylation plays a pivotal role in regulating mitochondrial fission-fusion dynamics, we established stable DLAT-knockdown HEK293T cells using lentiviral shRNA and reconstituted them with either wild-type DLAT (WT-DLAT) or lipoylation-deficient mutants (K132R, K259R, or K132/259R)—key residues previously identified as DLAT lipoylation sites[43]. Western blotting analysis demonstrated that WT-DLAT, but not the K132R or K259R mutants, restored the expression of OPA1 (a fusion mediator) and p-DRP1^{Ser637} (an inhibitory fission marker), confirming that lipoylation at these sites is essential for DLAT's regulation of mitochondrial dynamics (Fig. 5A). To further assess the functional consequences of DLAT lipoylation, we performed comprehensive mitochondrial analyses, including morphology assessment, MMP measurement, and cristae ultrastructure evaluation. Consistent with the rescue results, WT-DLAT-expressing cells displayed elongated mitochondrial networks, stable MMP, and well-organized cristae. In contrast, cells harboring K132R or K259R mutants exhibited fragmented mitochondria, depolarized MMP, and disrupted cristae, reinforcing the necessity of lipoylation for mitochondrial integrity

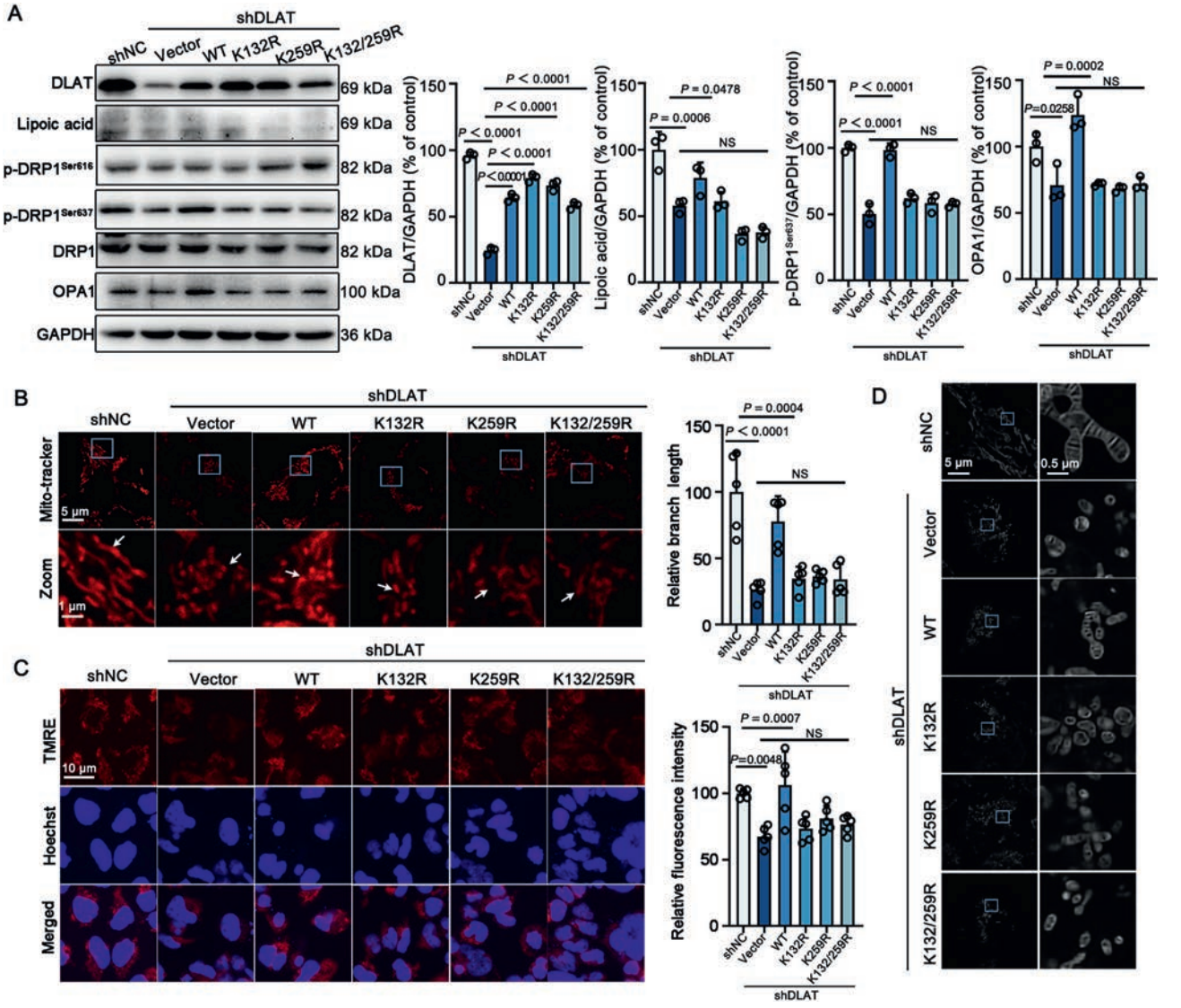

Figure 5 Lipoylation of DLAT at K132 and K259 is essential for mitochondria fusion. (A) Western blotting analysis of DLAT-knockdown HEK293T cells rescued with either WT-DLAT or lipoylation-deficient mutants ($n = 3$ independent experiments). (B) Confocal microscopy of mitochondria stained with Mito-tracker in DLAT-knockdown cells reconstituted with the indicated plasmids ($n = 5$ images). (C) MMP assessed by TMRE staining in rescued cells ($n = 5$ images). (D) Ultrastructural analysis of mitochondrial cristae *via* PKMO staining ($n = 3$ images). The data are presented as mean ± SD. Multiple group comparisons were evaluated through one-way analysis of variance (ANOVA). $P < 0.05$ was considered statistically significant. NS, no statistical difference.

(Fig. 5B−D). Taken together, these findings conclusively establish DLAT lipoylation as indispensable for maintaining mitochondrial homeostasis.

3.5. Rhy rescues mitochondrial bioenergetics and neurotransmitter recycling by activating DLAT-mediated metabolic pathways

To systematically investigate DLAT knockdown-induced downstream alterations and their functional consequences, we conducted proteomic profiling integrated with comprehensive bioinformatic analyses. Volcano plot visualization revealed extensive proteome-wide changes in DLAT-deficient cells versus controls (Fig. 6A), with the top 20 most differentially expressed proteins (10 upregulated and 10 downregulated) cataloged in Supporting Information Fig. S6. KEGG pathway enrichment analysis of the 15 most significantly perturbed pathways uncovered substantial disturbances in energy metabolism and stress-responsive signaling cascades (Fig. 6B and E). Notably impaired pathways included the TCA cycle, AMPK signaling, and FOXO signaling networks, directly reflecting DLAT's canonical function as a metabolic nexus regulating mitochondrial acetyl-CoA homeostasis. Gene Ontology (GO) analysis demonstrated significant enrichment in mitochondrial matrix and synaptic vesicles (Fig. 6C and D), underscoring DLAT's dual regulatory capacity in both bioenergetics and neuronal transmission. Substantiating these observations, Western blotting analysis documented that Rhy treatment markedly increased p-AMPKα (Thr172), FOXO3, p-STAT3, and p-EGFR expression (Fig. 6F and G). Importantly, Rhy treatment effectively rescued expression of critical vesicular transport machinery components (KIF5B, KIF5C, KIF1B, and VMAT2) that govern synaptic vesicle trafficking and dopaminergic neurotransmission (Fig. 6H and I). Collectively, these multimodal datasets provide compelling evidence that Rhy-mediated DLAT activation coordinately restores mitochondrial metabolic competence and neurotransmitter recycling capacity.

3.6. Rhy mitigates 6-OHDA-induced mitochondrial dysfunction and neurotoxicity in vivo

Our investigation commenced with pharmacokinetic analyses confirming Rhy's favorable oral bioavailability and efficient brain penetration, with peak plasma concentrations (t_{max}) attained at 1 h post-administration (Supporting Information Fig. S7A and S7B). Rhy demonstrated dose-proportional pharmacokinetics in both plasma and brain tissue compartments (Fig. S7C and S7D). Building upon these findings, we evaluated Rhy's therapeutic efficacy in a unilateral striatal 6-OHDA-lesioned PD mouse model. After 1 week post-lesion, mice exhibiting robust motor impairments (>5 contralateral rotations/min) were randomized into vehicle, Rhy (5, 10, and 20 mg/kg), or Madopar-treated groups (Fig. 7A). Following three weeks of treatment, Rhy administration dose-dependently improved motor coordination, restored muscular strength, and significantly attenuated apomorphine-evoked rotational asymmetry (Fig. 7B−D). These behavioral benefits paralleled substantial neurochemical restoration, evidenced by normalized striatal dopamine and DOPAC levels (Fig. 7E and F). Importantly, immunohistochemical (IHC) analyses substantiated Rhy's neuroprotective effects through preserved tyrosine hydroxylase expression within nigral dopaminergic neurons and their striatal terminals (Fig. 7G−K).

Consistent with our cellular findings, TEM analysis revealed that Rhy treatment reversed 6-OHDA-induced mitochondrial fragmentation and cristae disruption in nigral dopaminergic neurons (Fig. 8A). Western blotting analysis further demonstrated that Rhy promoted mitochondrial fusion *in vivo*, as indicated by upregulated p-DRP1^{Ser637}, MFN2, and OPA1 expression (Fig. 8B and C). Notably, Rhy significantly reduced DLAT-SIRT4 colocalization in the SN (Fig. 8D and E) while enhancing protein lipoylation, suggesting an interplay between mitochondrial dynamics and lipoylation-dependent regulation. Collectively, these findings demonstrate that Rhy alleviates motor deficits and mitochondrial pathology in PD mice by restoring mitochondrial homeostasis and protecting dopaminergic neurons.

Building on these promising efficacy data, we then performed a comprehensive toxicological assessment to evaluate the safety of Rhy administration. A comprehensive toxicological evaluation revealed no evidence of organ toxicity, as determined by histopathological analysis (HE staining) of major organs (Supporting Information Fig. S8A). Furthermore, evaluation of renal and hepatic function markers, including aspartate aminotransferase (AST), alanine aminotransferase (ALT), albumin, urea, and albumin/globulin (A/G) ratio (Fig. S8B−S8F) showed no significant alterations at therapeutic doses. Additional acute toxicity testing demonstrated median lethal dose (LD_{50}) exceeding 1000 mg/kg, with no observed mortality or acute neurological toxicity at effective doses. These findings collectively indicate that Rhy possesses a favorable safety profile within the therapeutic dose range, supporting its potential as a neuroprotective agent for PD treatment.

3.7. Rhy exerted neuroprotective effects in A53T transgenic mice

To further evaluate Rhy's therapeutic potential, we treated 7-month-old A53T transgenic mice (C57BL/6 J background). After 6 weeks of daily Rhy treatment (10 mg/kg), the mice showed significant improvement in PD-associated motor dysfunction, including enhanced motor coordination, grip strength, and locomotor activity (Fig. 9A−F). As expected in PD pathology, vehicle-treated A53T mice exhibited severe dopaminergic neuron degeneration in both the SN and striatum, characterized by reduced TH-positive neuron counts (Fig. 9G and H) and decreased TH protein expression (Fig. 9J, Supporting Information Fig. S9A). Crucially, Rhy administration effectively reversed these neurodegenerative changes, increasing both TH-positive neuron numbers and TH/GAPDH protein levels. Furthermore, Rhy treatment significantly reduced pathological A53T α-syn accumulation in the SN, as confirmed by IHC staining and Western blotting analysis (Fig. 9I and J, Fig. S9B). Importantly, mechanistic investigation revealed a disease-associated downregulation of DLAT protein expression in A53T mouse brains (Supporting Information Fig. S10). Taken together, these findings demonstrate that Rhy ameliorates both behavioral and neuropathological phenotypes in this PD mouse model, potentially through its modulation of DLAT expression.

3.8. DLAT orchestrates neuronal dysfunction in PD pathogenesis

To elucidate the clinical relevance of DLAT in PD, we systematically analyzed single-cell RNA sequencing data from the SN of PD patients and healthy controls retrieved from the GEO database

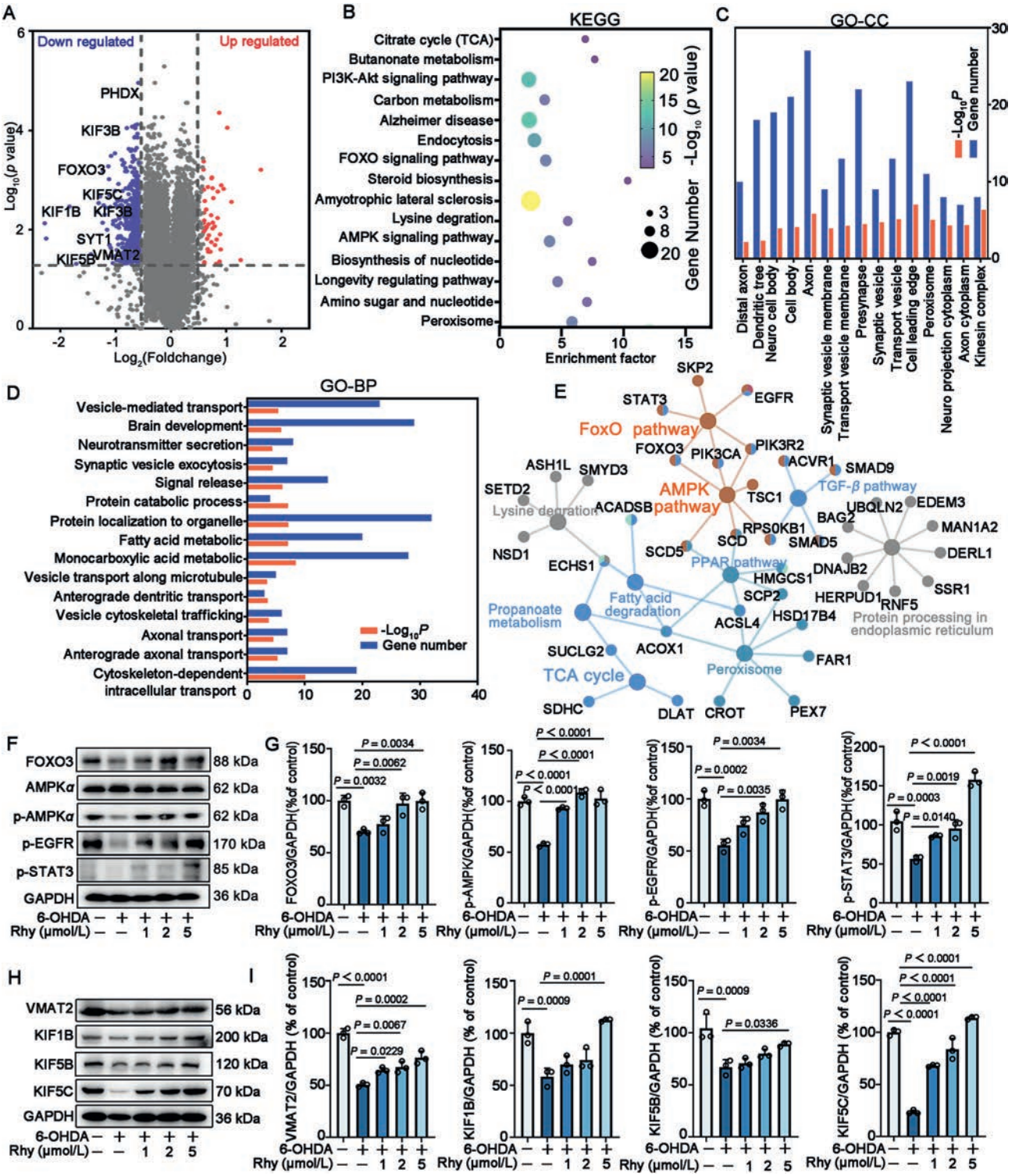

Figure 6 Rhy enhances DLAT to regulate mitochondrial energy metabolism and neurotransmitter recycling. (A) Differential gene expression analysis by proteomic profiling following DLAT knockdown (volcano plot). (B) Top 15 enriched KEGG pathways altered upon DLAT depletion. (C) Subcellular distribution of DLAT-regulated proteins (GO cellular component analysis). (D) Functional categorization of DLAT-dependent biological processes (top 15 GO terms). (E) Pathway interaction network identified by ClueGO-based KEGG enrichment. (F, G) Western blotting detection of metabolic signaling proteins (p-AMPKα, FOXO3a) and receptor tyrosine kinase activation markers (p-STAT3, p-EGFR) in Rhy-treated PC12 cells (24 h, $n = 3$). (H, I) Western blotting analysis of neuronal transport machinery components (KIF5B/C, KIF1B, VMAT2) in Rhy-treated PC12 cells (24 h, $n = 3$). The data are presented as mean ± SD. Multiple group comparisons were evaluated through one-way analysis of variance (ANOVA). $P < 0.05$ was considered statistically significant.

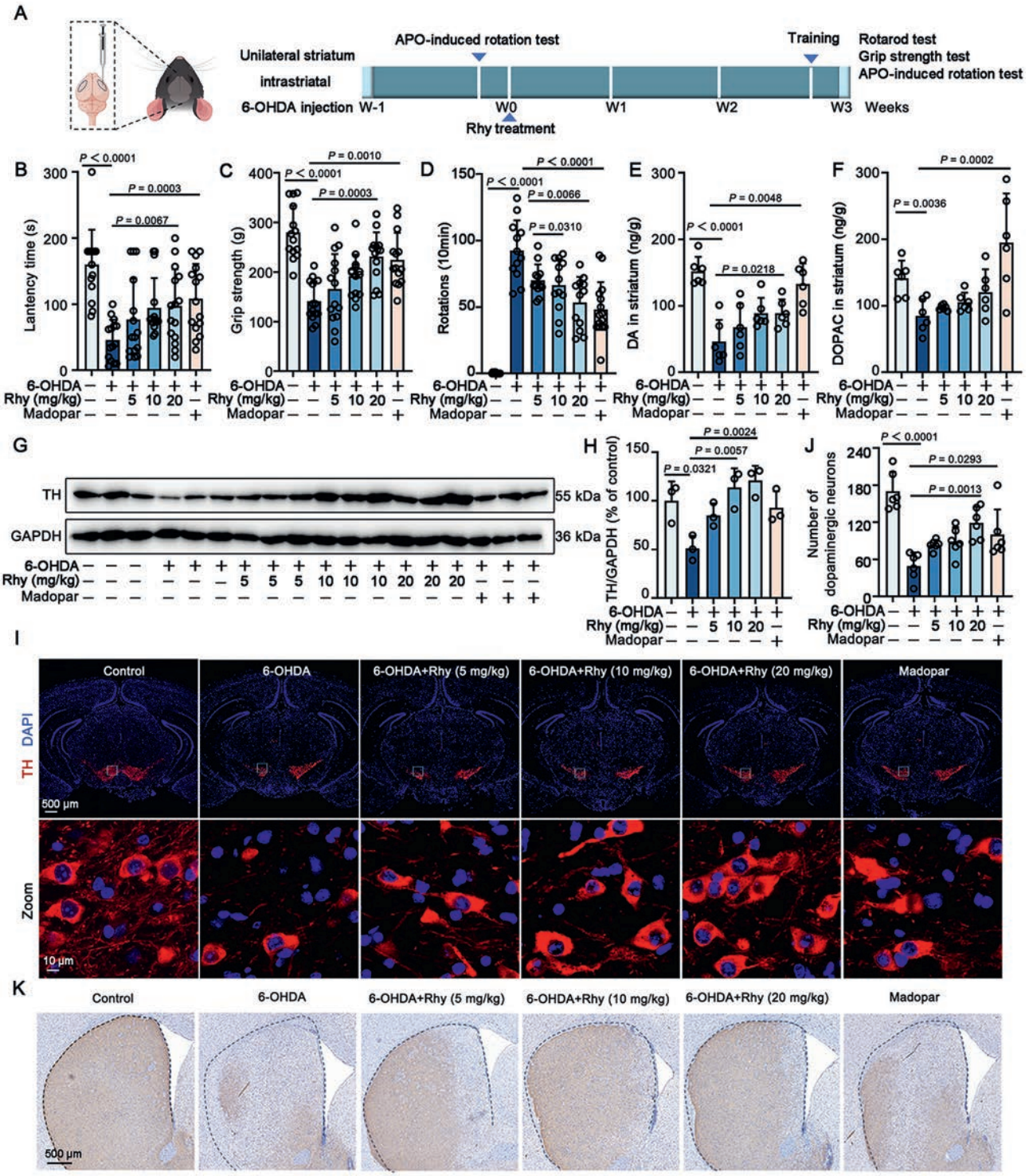

Figure 7 Rhy mitigates 6-OHDA-induced mitochondrial dysfunction and neurotoxicity *in vivo*. (A) Schematic overview of the experimental timeline, including unilateral intrastriatal 6-OHDA lesioning and subsequent treatment. (B) Motor coordination was evaluated by rotarod latency ($n = 14$ mice/group). (C) Neuromuscular function was assessed by grip strength ($n = 14$ mice/group). (D) Dopaminergic asymmetry was measured by apomorphine-induced contralateral rotations ($n = 12$ mice/group). (E, F) Quantification of DA and DOPAC levels in the striatum using UPLC−MS ($n = 6$ mice/group). (G−J) Western blot ($n = 3$ mice/group) and immunofluorescence analysis of TH expression in the substantia nigra ($n = 6$ mice/group). (K) Representative images of TH immunohistochemical staining in the striatum ($n = 3$ mice/group). The data are presented as mean ± SD. Multiple group comparisons were evaluated through one-way analysis of variance (ANOVA). $P < 0.05$ was considered statistically significant.

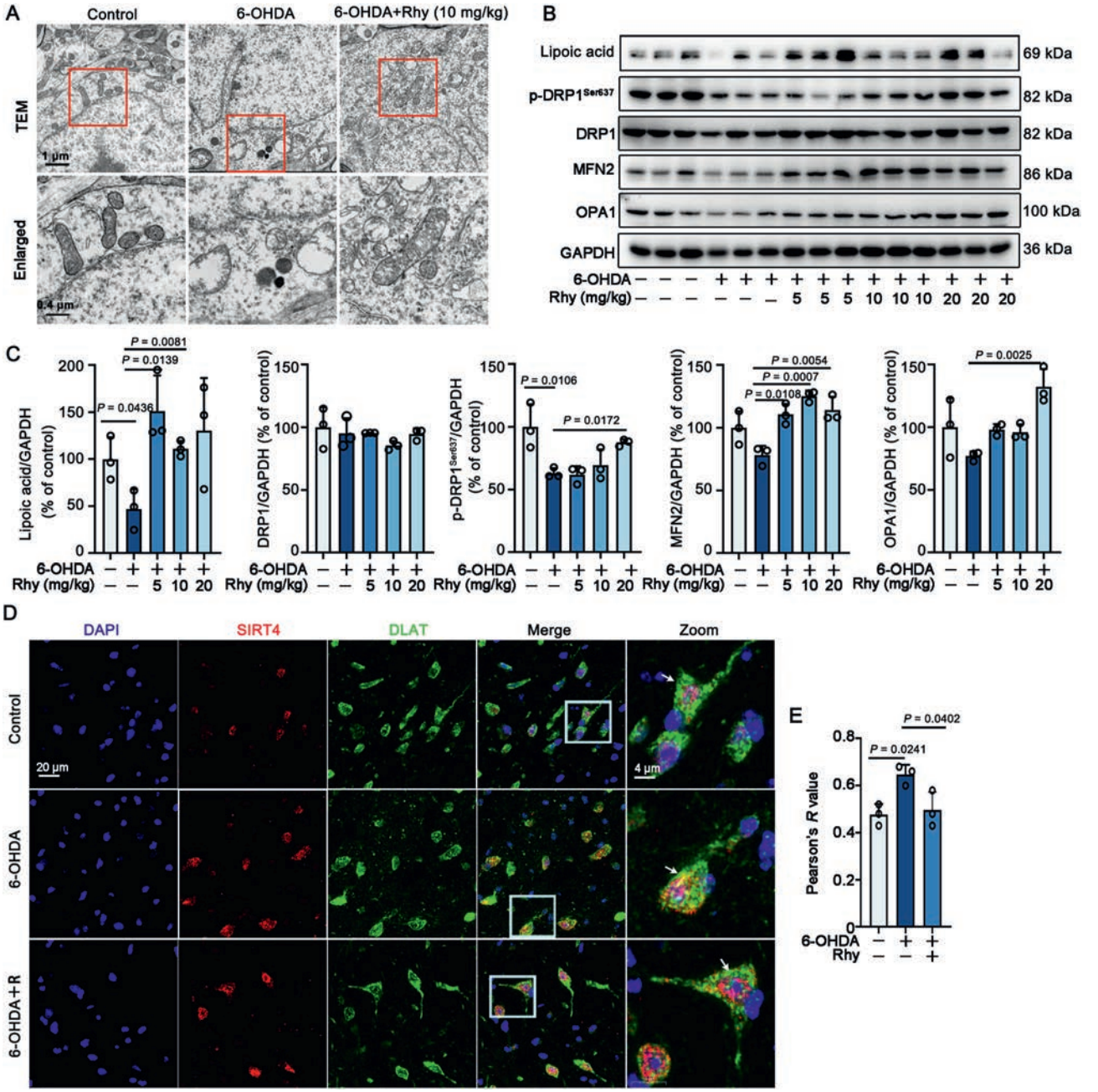

Figure 8 Rhy ameliorates mitochondrial dysfunction *via* suppression of the DLAT−SIRT4 axis in PD mice. (A) Representative transmission electron microscope images illustrating mitochondrial ultrastructure in substantia nigra neurons. (B, C) Protein levels of mitochondrial dynamics markers (DRP1, p-DRP1^{Ser616}, p-DRP1^{Ser637}, MFN2, OPA1) in SN tissues were analyzed by Western blotting ($n = 3$). (D, E) Immunofluorescence co-staining demonstrating reduced DLAT−SIRT4 colocalization in substantia nigra following Rhy treatment ($n = 3$). The data are presented as mean ± SD. Multiple group comparisons were evaluated through one-way analysis of variance (ANOVA). $P < 0.05$ was considered statistically significant.

(GSE243639). The clinical characteristics of the subjects were summarized in Supporting Information Fig. S11. The cellular composition of the SN included oligodendrocytes (32.97%), oligodendrocyte precursor cells (6.69%), microglia (14.52%), neurons (21.52%), astrocytes (19.28%), vascular endothelial cells (4.22%), and other cell populations (0.8%) (Fig. 10A and B). Notably, neuronal populations exhibited the most pronounced depletion in PD patients compared to other cell types (Fig. 10C). Further analysis revealed DLAT's distinct cell type-specific expression pattern, with pronounced enrichment in neurons relative to non-neuronal populations (Fig. 10D). Crucially, DLAT expression at the transcript level was markedly reduced within the neuronal populations of PD patients compared to healthy individuals (Fig. 10E). Analysis of public proteomics data (PRIDE: PXD000427) corroborated this finding, confirming that DLAT protein abundance was also significantly decreased in the SN of

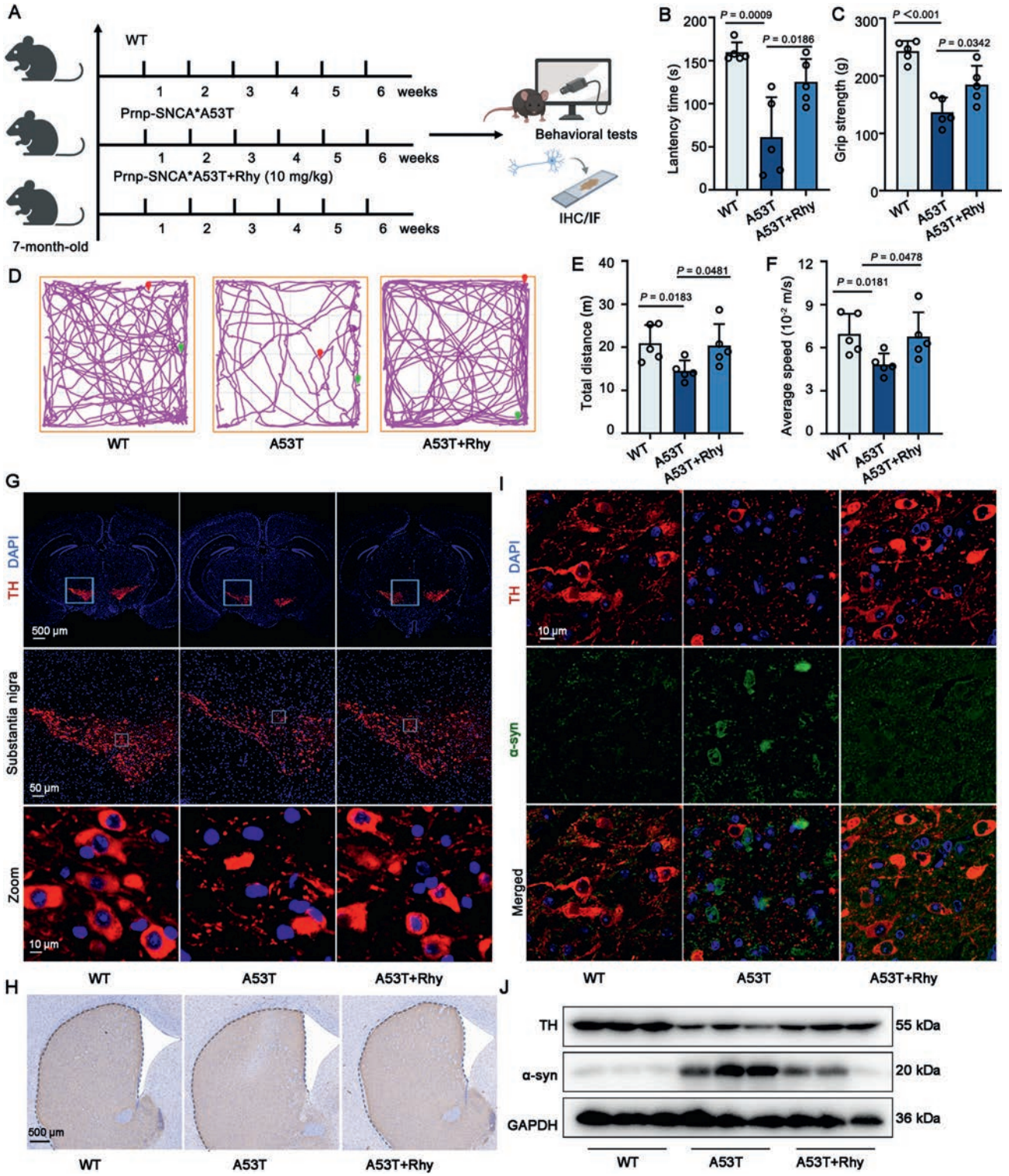

Figure 9 Rhy treatment ameliorates motor deficits and neuropathology in A53T transgenic mice. (A) Schematic overview of the experimental timeline. (B) Motor coordination was assessed by the rotarod test ($n = 5$ mice/group). (C) Muscle strength was evaluated using a grip strength test ($n = 5$ mice/group). (D−F) Spontaneous locomotor activity was analyzed by open-field test. Representative movement traces (D), total distance traveled (E), and average speed (F), $n = 5$ mice/group. (G) TH immunofluorescence staining in the substantia nigra. (H) TH IHC staining in striatum. (I) Double IHC staining of α-syn (green) and TH (red) in the substantia nigra. (J) Western blotting analysis of TH and α-syn expression in midbrain ($n = 3$ mice/group). The data are presented as mean ± SD. Multiple group comparisons were evaluated through one-way analysis of variance (ANOVA). $P < 0.05$ was considered statistically significant.

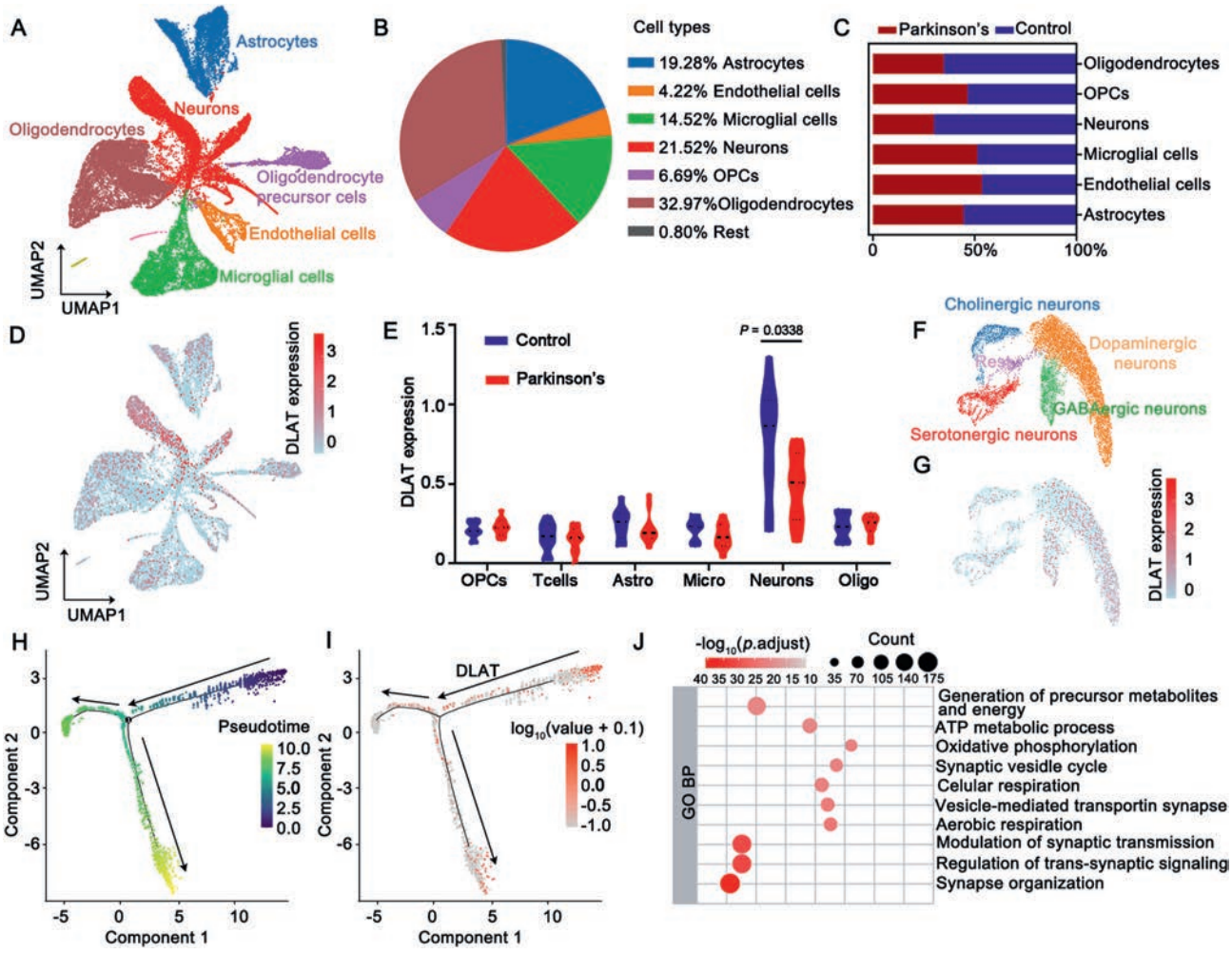

Figure 10 Single-nucleus RNA sequencing (snRNA-seq) identifies cell type-specific DLAT expression reductions in the substantia nigra pars compacta (SNpc) of PD patients. (A) UMAP visualization of 33,904 high-quality nuclei from three PD and three control postmortem SNpc samples. (B) Proportional distribution of major cell populations within the SNpc dataset (pie chart). (C) Cluster-wise quantification of nuclei derived from control *versus* PD donors (bar plot). (D) Neuron-specific enrichment of DLAT expression across all cell types. (E) Significant downregulation of DLAT mRNA levels in PD-derived SNpc neurons compared to controls. (F) Subclustering analysis of neuronal populations from panel A. (G) Elevated DLAT expression in dopaminergic and GABAergic neuronal subpopulations. (H, I) Pseudotemporal trajectory reconstruction (Monocle 2) depicting neuronal developmental dynamics (H) with corresponding DLAT expression patterns (I). (J) GO biological process enrichment analysis (top 10 terms) differentiating PD and control SNpc neurons. The data are presented as mean ± SD. Multiple group comparisons were evaluated through one-way analysis of variance (ANOVA). $P < 0.05$ was considered statistically significant.

PD patients (Supporting Information Fig. S12A and S12B). These results highlight the dysregulation of DLAT and underscore its potential as a therapeutic target for PD.

Subsequent subclustering of neuronal populations identified preferential DLAT expression in dopaminergic neurons (Fig. 10F and G), establishing DLAT as a critical determinant of dopaminergic neuronal function. Pseudotemporal trajectory uncovered dynamic DLAT expression patterns along the inferred neuronal transcriptional trajectory, characterized by relatively higher expression observed at both early and late pseudotime states (Fig. 10H and I). This expression pattern closely paralleled metabolic transitions, wherein upregulated DLAT met enhanced bioenergetic requirements during neuronal proliferation, while its sustained expression preserved critical ATP-driven functions in mature neurons, particularly neurotransmitter synthesis and synaptic vesicle release in dopaminergic populations. GO enrichment analysis of PD-associated transcriptional alterations highlighted significant convergence on DLAT-regulated pathways, particularly ATP metabolism, oxidative phosphorylation, and synaptic vesicle cycling, each functionally reliant on DLAT-driven pyruvate decarboxylation (Fig. 10J). Collectively, these findings implicate DLAT deficiency in PD pathogenesis, likely through compromised mitochondrial metabolic support in energy-demanding dopaminergic neurons.

4. Discussion

PD, the second most prevalent neurodegenerative disorder worldwide, exhibits an age-dependent incidence escalating from ~1% at age 65 to nearly 5% by age 85[46,47]. Current therapeutic strategies predominantly address symptom management through surgical approaches and pharmacological interventions, like

Levodopa, which is a mainstream medication for the treatment of PD[48]. Although Levodopa predominantly alleviates motor symptoms, it fails to halt progressive neuronal loss. Consequently, a mechanistic understanding of PD pathogenesis is urgently needed for developing disease-modifying treatments.

Mitochondrial dysfunction is known to play a central role in PD pathogenesis. Mitochondria undergo morphological changes, such as fission and fusion, to repair damaged mitochondria and ensure the quality of mitochondria. However, in PD, the homeostatic balance of mitochondrial dynamics is perturbed, leading to the aberrant production of fragmented mitochondria, loss of MMP, reduced ATP production, elevated ROS levels, and increased oxidative stress. Therefore, targeting mitochondrial dynamics presents a promising direction for the treatment of PD. Actually, DRP1 inhibitors have been explored as a therapeutic avenue in PD. Mdivi-1, a quinazolinone that binds allosterically to DRP1, suppresses its GTPase activity by preventing the oligomerization of DRP1 ring structures, thereby attenuating pathological mitochondrial fission[49]. Moreover, Mdivi-1 enhances dopamine release and neuronal survival in the MPTP-induced mouse model[50], as well as mitigates motor deficits and neurodegeneration in A53T-α-syn transgenic rats[51]. Beyond small molecules, rationally designed peptides like P110 inhibit DRP1 activity in MPTP toxicity models and further rescue mitochondrial dysfunction by stabilizing MMP and curbing superoxide overproduction[52]. On review, it seems that DRP1 inhibition-based therapies may seem promising, while critical questions persist regarding long-term safety and tissue selectivity. Chronic effects of DRP1 modulation remain uncharacterized, and off-target consequences, particularly in non-neuronal systems, warrant systematic investigation. These challenges highlight the need for novel modulators, especially from natural products that combine structural diversity and evolutionarily optimized safety. Here, our findings established Rhy, a bioactive alkaloid from *Uncaria* species, exemplifying this potential by balancing mitochondrial fusion and fission with inherent biocompatibility. Rhy is bound to the L domain of DLAT, allosterically disrupting its interaction with sirtuin 4 (SIRT4) and subsequently enhancing DLAT lipoylation, thereby restoring fusion/fission balance.

DLAT, a core component of the PDC, is well-known for its metabolic role in the TCA cycle[53]. Our study, however, reveals a novel function for DLAT in mitochondrial dynamics, as its knockout in cells caused pronounced mitochondrial fragmentation. While the precise mechanism is still under investigation, we propose that DLAT governs mitochondrial dynamics indirectly through its canonical metabolic function. By maintaining PDC activity, DLAT ensures the production of acetyl-CoA, ATP, and a stable redox balance—all of which are critical for energy-dependent mitochondrial fusion. This model is strongly supported by evidence that inhibiting PDC promotes excessive fission[54], while activating it enhances mitochondrial fusion and energy metabolism[55]. Thus, DLAT acts as a critical metabolic hub where its role in the TCA cycle is directly linked to mitochondrial quality control, suppressing pathological fission by ensuring robust energy production in both health and disease. This raises the high possibility that changes in DLAT expression could serve as a biomarker for neurodegenerative diseases, particularly PD. Our analysis of a public proteomics dataset from the human SN (PRIDE: PXD000427) revealed that DLAT protein abundance was significantly lower in PD patients compared to healthy elderly individuals (Fig. S12A and S12B). Furthermore, the dataset (PRIDE: PXD051145) revealed a dramatic 90% reduction in DLAT protein levels in elderly individuals (mean age, 83.9) compared to the young (mean age, 28.7) and middle-aged (mean age, 62.3) groups (Fig. S12C). This positions DLAT as a potential candidate for the biomarkers of neurodegenerative progression.

Importantly, lipoylation modification of DLAT is essential for maintaining its functional integrity, highlighting the significance of PTM in DLAT-mediated mitochondrial regulation. Protein lipoylation is an essential PTM for mitochondrial enzymes and is conserved in only five human proteins, including DLAT, DLST, DBT, and GCSH[56,57]. In this study, we found that lipoylation of DLAT was decreased in the 6-OHDA-induced PD model, thereby impacting mitochondrial energy metabolism. Also, studies by Grassi et al.[58] revealed that α-syn aggregates reduce mitochondrial lipoylation and induce mitochondrial fragmentation, ATP depletion, and oxidative stress. These indicate that lipoylation may play a role in the pathological pathways of PD. Beyond PD, lipoylation is also closely linked to aging[59]. Lipoylation also influences other pathways, such as fatty acid oxidation and branched-chain amino acid degradation. These results open up the possibility of alleviating age-associated decline in energy expenditure by enhancing the mitochondrial lipoylation pathway, like α-lipoic acid supplementation or pharmacological modulation of lipoylation-modifying enzymes, offering a potential therapeutic strategy for PD.

SIRT4 is a member of the mammalian NAD^+-dependent deacetylase enzyme family, which regulates a variety of biological processes, including genomic regulation, stress responses, mitochondrial metabolic homeostasis, and aging[60]. However, unlike other SIRTs in this family, SIRT4 exhibits low deacetylase activity but possesses robust delipoylase activity. It enzymatically hydrolyzes the lipoamide cofactor of DLAT, thereby reducing PDC activity[45]. In our study, Rhy was found to inhibit the interaction between SIRT4 and DLAT, leading to enhanced mitochondrial energy metabolism accompanied by increased PDC enzyme activity. Importantly, single-cell transcriptomics revealed elevated SIRT4 protein levels in the SN of PD patients, consistent with recent findings showing that SIRT4 expression in the brain's preoptic region also increases with age[61]. Knockdown of SIRT4 in cellular and animal models of Alzheimer's disease significantly reduces neuronal apoptosis[62]. Another study demonstrated that SIRT4 levels are elevated in oocytes of aged mice, and SIRT4 knockout partially rescues the defective phenotypes in these oocytes[63], while overexpression of SIRT4 in mouse oocytes results in increased ROS levels, reduced ATP production, and mitochondrial damage[64]. Beyond its role in aging, most studies to date have confirmed SIRT4's tumor-suppressive functions[65], which may stem from its inhibitory effects on mitochondrial energy metabolism, particularly through its modulation of lipoylation levels. However, the relationship between SIRT4 and mitochondrial energy metabolism remains controversial, as some studies suggest that SIRT4 has anti-aging properties and contributes to maintaining normal mitochondrial function. Therefore, further in-depth research on SIRT4 is warranted to elucidate its multifaceted roles.

Overall, therapeutic approaches targeting mitochondrial dynamics, including the use of compounds like Rhy, have demonstrated the potential to restore mitochondrial function. By bolstering lipoylation-dependent metabolic flexibility, such interventions may counteract age-related bioenergetic decline and PD progression. Thus, future efforts can prioritize exploring the feasibility of taking DLAT as a PD target in clinical lipoylation-

enhancing adjuvants and emphasizing mitochondrial resilience as an anti-aging treatment.

5. Conclusions

In this study, we demonstrated that Rhy mitigated 6-OHDA-induced mitochondrial dysfunction by promoting mitochondrial fusion and uncovered DLAT as the direct molecular target underlying Rhy-mediated regulation of mitochondrial dynamics. Mechanistically, Rhy binds to the N-terminal lipoyl domain of DLAT, allosterically disrupting its interaction with SIRT4 and subsequently enhancing DLAT lipoylation, thereby rescuing energy metabolism and enhancing mitochondrial fusion. Taken together, our results not only validate the therapeutic feasibility of modulating mitochondrial dynamics by Rhy in PD but also pinpoint DLAT as a druggable target with translational potential.

Acknowledgments

This work was financially supported by the National Natural Science Foundation of China of China (Nos.: 82574548, 82173951, 82325050, and 82174008), China Postdoctoral Science Foundation (2024M760160), Beijing Municipal Natural Science Foundation-Key Research Project of the Daxing (L246029, China), Jinan New 20 Policies for Higher Education Funding (202228048 China), and the Special Fund for "Tian-Chi Talent Introduction Program".

Author contributions

Xiaomin Liang: Writing-original draft, Investigation, Formal analysis, Data curation. Xunfang Yang: Investigation, Data curation. Shuhui Wang: Investigation, Data curation. Fangfang Zhuo: Investigation. Xingzi Hou: Investigation, Data curation. Pengfei Tu: Supervision, Conceptualization. Yang Liu: Writing-review and editing, Conceptualization. Kewu Zeng: Writing-review and editing, Supervision, Project administration, Conceptualization. Qingying Zhang: Writing-review and editing, Supervision, Project administration, Funding acquisition, Conceptualization.

Conflicts of interest

The authors declare no conflicts of interest.

Appendix A. Supporting information

Supporting information to this article can be found online at https://doi.org/10.1016/j.apsb.2026.06.016.

References

1. Postuma RB, Berg D, Stern M, Poewe W, Olanow CW, Oertel W, et al. MDS clinical diagnostic criteria for Parkinson's disease. *Mov Disord* 2015;**30**:1591−601.
2. Kalia LV, Lang AE. Parkinson's disease. *Lancet* 2015;**386**:896−912.
3. Poewe W, Seppi K, Tanner CM, Halliday GM, Brundin P, Volkmann J, et al. Parkinson's disease. *Nat Rev Dis Primers* 2017;**3**:17013.
4. Shang M, Ning J, Zang C, Ma J, Yang Y, Jiang Y, et al. FLZ attenuates Parkinson's disease pathological damage by increasing glycoursodeoxycholic acid production *via* down-regulating *Clostridium innocuum*. *Acta Pharm Sin B* 2025;**15**:973−90.
5. Henrich MT, Oertel WH, Surmeier DJ, Geibl FF. Mitochondrial dysfunction in Parkinson's disease—a key disease hallmark with therapeutic potential. *Mol Neurodegener* 2023;**18**:83.
6. Brand MD, Nicholls DG. Assessing mitochondrial dysfunction in cells. *Biochem J* 2011;**435**:297−312.
7. Vafai SB, Mootha VK. Mitochondrial disorders as windows into an ancient organelle. *Nature* 2012;**491**:374−83.
8. Duchen MR. Mitochondria and calcium: from cell signaling to cell death. *J Physiol* 2000;**529**:57−68.
9. Connolly NMC, Theurey P, Adam-Vizi V, Bazan NG, Bernardi P, Bolaños JP, et al. Guidelines on experimental methods to assess mitochondrial dysfunction in cellular models of neurodegenerative diseases. *Cell Death Differ* 2018;**25**:542−72.
10. Cai Q, Tammineni P. Alterations in mitochondrial quality control in Alzheimer's disease. *Front Cell Neurosci* 2016;**10**:24.
11. Xu J, Du W, Zhao Y, Lim K, Lu L, Zhang C, et al. Mitochondria targeting drugs for neurodegenerative diseases—design, mechanism and application. *Acta Pharm Sin B* 2022;**12**:2778−89.
12. Burns RS, Chiueh CC, Markey SP, Ebert MH, Jacobowitz DM, Kopin IJ. A primate model of parkinsonism: selective destruction of dopaminergic neurons in the pars compacta of the SN by *N*-methyl-4-phenyl-1,2,3,6-tetrahydropyridine. *Proc Natl Acad Sci U S A* 1983;**80**:4546−50.
13. Rojo AI, Montero C, Salazar M, Close RM, Fernández Ruiz J, Sánchez González MA, et al. Persistent penetration of MPTP through the nasal route induces Parkinson's disease in mice. *Eur J Neurosci* 2006;**24**:1874−84.
14. Panov A, Dikalov S, Shalbuyeva N, Taylor G, Sherer T, Greenamyre JT. Rotenone model of Parkinson disease: multiple brain mitochondria dysfunctions after short term systemic rotenone intoxication. *J Biol Chem* 2005;**280**:42026−35.
15. Chia SJ, Tan EK, Chao YX. Historical Perspective: models of Parkinson's disease. *Int J Mol Sci* 2020;**21**:2464.
16. Kitada T, Asakawa S, Hattori N, Matsumine H, Yamamura Y, Minoshima S, et al. Mutations in the *parkin* gene cause autosomal recessive juvenile parkinsonism. *Nature* 1998;**392**:605−8.
17. Valente EM, Abou Sleiman PM, Caputo V, Muqit MM, Harvey K, Gispert S, et al. Hereditary early-onset Parkinson's disease caused by mutations in PINK1. *Science* 2004;**304**:1158−60.
18. Zimprich A, Biskup S, Leitner P, Lichtner P, Farrer M, Lincoln S, et al. Mutations in LRRK2 cause autosomal dominant Parkinsonism with pleomorphic pathology. *Neuron* 2004;**44**:601−7.
19. Varkuti BH, Liu Z, Kepiro M, Pacifico R, Gai Y, Kamenecka T, et al. High-throughput small molecule screen identifies modulators of mitochondrial function in neurons. *iScience* 2020;**23**:100931.
20. Ralto KM, Rhee EP, Parikh SM. NAD^+ homeostasis in renal health and disease. *Nat Rev Nephrol* 2020;**16**:99−111.
21. Brakedal B, Dölle C, Riemer F, Ma Y, Nido GS, Skeie GO, et al. The NADPARK study: a randomized phase I trial of nicotinamide riboside supplementation in Parkinson's disease. *Cell Metab* 2022;**34**:396−407.
22. Wang C, Du W, Su QP, Zhu M, Feng P, Li Y, et al. Dynamic tubulation of mitochondria drives mitochondrial network formation. *Cell Res* 2015;**25**:1108−20.
23. Youle RJ, van der Bliek AM. Mitochondrial fission, fusion, and stress. *Science* 2012;**337**:1062−5.
24. Chen H, Chan DC. Mitochondrial dynamics—fusion, fission, movement, and mitophagy—in neurodegenerative diseases. *Hum Mol Genet* 2009;**18**:R169−76.
25. Liu R, Chan DC. The mitochondrial fission receptor Mff selectively recruits oligomerized Drp1. *Mol Biol Cell* 2015;**26**:4466−77.
26. Archer SL. Mitochondrial dynamics-mitochondrial fission and fusion in human diseases. *N Engl J Med* 2013;**369**:2236−51.
27. Flippo KH, Lin Z, Dickey AS, Zhou X, Dhanesha NA, Walters GC, et al. Deletion of a neuronal Drp 1 activator protects against cerebral ischemia. *J Neurosci* 2020;**40**:3119−29.
28. Santel A, Fuller MT. Control of mitochondrial morphology by a human mitofusin. *J Cell Sci* 2001;**114**:867−74.

29. Gao S, Hu J. Mitochondrial fusion: the machineries in and out. *Trends Cell Biol* 2021;**31**:62−74.
30. Gomez-Lazaro M, Bonekamp NA, Galindo MF, Jordán J, Schrader M. 6-Hydroxydopamine (6-OHDA) induces Drp 1-dependent mitochondrial fragmentation in SH-SY5Y cells. *Free Radic Biol Med* 2008;**44**: 1960−9.
31. Wang X, Su B, Liu W, He X, Gao Y, Castellani RJ, et al. DLP1-dependent mitochondrial fragmentation mediates 1-methyl-4-phenylpyridinium toxicity in neurons: implications for Parkinson's disease. *Aging Cell* 2011;**10**:807−23.
32. Otmani A, Jóhannesson G, Brautaset R, Tribble JR, Williams PA. Prophylactic nicotinamide treatment protects from rotenone-induced neurodegeneration by increasing mitochondrial content and volume. *Acta Neuropathol Commun* 2024;**12**:37.
33. Yang Y, Ouyang Y, Yang L, Beal MF, McQuibban A, Vogel H, et al. Pink 1 regulates mitochondrial dynamics through interaction with the fission/fusion machinery. *Proc Natl Acad Sci U S A* 2008;**105**: 7070−5.
34. Poole AC, Thomas RE, Andrews LA, McBride HM, Whitworth AJ, Pallanck LJ. The PINK1/Parkin pathway regulates mitochondrial morphology. *Proc Natl Acad Sci U S A* 2008;**105**:1638−43.
35. Yu W, Sun Y, Guo S, Lu B. The PINK1/Parkin pathway regulates mitochondrial dynamics and function in mammalian hippocampal and dopaminergic neurons. *Hum Mol Genet* 2011;**20**:3227−40.
36. Lee CJ, Hsueh TY, Lin LC, Tsai TH. Determination of protein-unbound rhynchiphylline brain distribution by microdialysis and ultra-performance liquid chromatography with tandem mass spectrometry. *Biomed Chromatogr* 2014;**28**:901−6.
37. Zhang YN, Yang YF, Xu W, Yang XW. The blood−brain barrier permeability of six indole alkaloids from *Uncariae Ramulus Cum Uncis* in the MDCK-pHaMDR cell monolayer model. *Molecules* 2017;**22**:1944.
38. Tian X, Xu Z, Chen M, Hu P, Liu F, Sun Z, et al. Simultaneous determination of eight bioactive compounds by LC−MS/MS and its application to the pharmacokinetics, liver first-pass effect, liver and brain distribution of orally administrated Gouteng-Baitouweng (GB) in rats. *J Chromatogr, B: Anal Technol Biomed Life Sci* 2018;**1084**: 122−31.
39. Geetha RG, Ramachandran S. Recent advances in the anti-inflammatory activity of plant-derived alkaloid rhynchophylline in neurological and cardiovascular diseases. *Pharmaceutics* 2021;**13**: 1170.
40. Geng H, Chen X, Wang C. Systematic elucidation of the pharmacological mechanisms of Rhynchophylline for treating epilepsy *via* network pharmacology. *BMC Complement Med Ther* 2021;**21**:9.
41. Zheng M, Chen M, Wang W, Zhou M, Liu C, Fan Y, et al. Protection by rhynchophylline against MPTP/MPP^+-induced neurotoxicity *via* regulating PI3K/Akt pathway. *J Ethnopharmacol* 2021;**268**:113568.
42. Zhang C, Xue Z, Zhu L, Zhou J, Zhuo L, Zhang J, et al. Rhynchophylline alleviates neuroinflammation and regulates metabolic disorders in a mouse model of Parkinson's disease. *Food Funct* 2023;**14**: 3208−19.
43. Prajapati S, Haselbach D, Wittig S, Patel MS, Chari A, Schmidt C, et al. Structural and functional analyses of the human PDH complex suggest a "Division-of-Labor" mechanism by local E1 and E3 clusters. *Structure* 2019;**27**:1124−36.
44. Chen S, Liu X, Peng C, Tan C, Sun H, Liu H, et al. The phytochemical hyperforin triggers thermogenesis in adipose tissue *via* a Dlat−AMPK signaling axis to curb obesity. *Cell Metab* 2021;**33**:565−80.
45. Mathias RA, Greco TM, Oberstein A, Budayeva HG, Chakrabarti R, Rowland EA, et al. Sirtuin 4 is a lipoamidase regulating pyruvate dehydrogenase complex activity. *Cell* 2014;**159**:1615−25.
46. De Lau LM, Breteler MM. Epidemiology of Parkinson's disease. *Lancet Neurol* 2006;**5**:525−35.
47. Van Den Eeden SK, Tanner CM, Bernstein AL, Fross RD, Leimpeter A, Bloch DA, et al. Incidence of Parkinson's disease: variation by age, gender, and race/ethnicity. *Am J Epidemiol* 2003; **157**:1015−22.
48. Jankovic J, Tan EK. Parkinson's disease: etiopathogenesis and treatment. *J Neurol Neurosurg Psychiatry* 2020;**91**:795−808.
49. Cassidy-Stone A, Chipuk JE, Ingerman E, Song C, Yoo C, Kuwana T, et al. Chemical inhibition of the mitochondrial division dynamin reveals its role in Bax/Bak-dependent mitochondrial outer membrane permeabilization. *Dev Cell* 2008;**14**:193−204.
50. Rappold PM, Cui M, Grima JC, Fan RZ, de Mesy-Bentley KL, Chen L, et al. Drp1 inhibition attenuates neurotoxicity and dopamine release deficits *in vivo*. *Nat Commun* 2014;**5**:5244.
51. Bido S, Soria FN, Fan RZ, Bezard E, Tieu K. Mitochondrial division inhibitor-1 is neuroprotective in the A53T-α-synuclein rat model of Parkinson's disease. *Sci Rep* 2017;**7**:7495.
52. Qi X, Qvit N, Su YC, Mochly-Rosen D. A novel Drp1 inhibitor diminishes aberrant mitochondrial fission and neurotoxicity. *J Cell Sci* 2013;**126**:789−802.
53. Patel MS, Roche TE. Molecular biology and biochemistry of pyruvate dehydrogenase complexes. *FASEB J* 1990;**4**:3224−33.
54. Tian L, Wu D, Dasgupta A, Chen KH, Mewburn J, Potus F, et al. Epigenetic metabolic reprogramming of right ventricular fibroblasts in pulmonary arterial hypertension: a pyruvate dehydrogenase kinase-dependent shift in mitochondrial metabolism promotes right ventricular fibrosis. *Circ Res* 2020;**126**:1723−45.
55. Oh CJ, Kim MJ, Lee JM, Kim DH, Kim IY, Park S, et al. Inhibition of pyruvate dehydrogenase kinase 4 ameliorates kidney ischemia-reperfusion injury by reducing succinate accumulation during ischemia and preserving mitochondrial function during reperfusion. *Kidney Int* 2023;**104**:724−39.
56. Solmonson A, DeBerardinis RJ. Lipoic acid metabolism and mitochondrial redox regulation. *J Biol Chem* 2018;**293**:7522−30.
57. Birsoy K, Wang T, Chen WW, Freinkman E, Abu Remaileh M, Sabatini DM. An essential role of the mitochondrial electron transport chain in cell proliferation is to enable aspartate synthesis. *Cell* 2015; **162**:540−51.
58. Grassi D, Howard S, Zhou M, Diaz Perez N, Urban NT, Guerrero Given D, et al. Identification of a highly neurotoxic α-synuclein species inducing mitochondrial damage and mitophagy in Parkinson's disease. *Proc Natl Acad Sci U S A* 2018;**115**: E2634−43.
59. Tajima K, Ikeda K, Chang HY, Chang CH, Yoneshiro T, Oguri Y, et al. Mitochondrial lipoylation integrates age-associated decline in brown fat thermogenesis. *Nat Metab* 2019;**1**:886−98.
60. Ji Z, Liu GH, Qu J. Mitochondrial sirtuins, metabolism, and aging. *J Genet Genomics* 2022;**49**:287−98.
61. Wong DW, Soga T, Parhar IS. Aging and chronic administration of serotonin-selective reuptake inhibitor citalopram upregulate Sirt4 gene expression in the preoptic area of male mice. *Front Genet* 2015;**6**:281.
62. Xing D, Zhang W, Cui W, Yao X, Xiao Y, Chen L, et al. SIRT4 promotes neuronal apoptosis in models of Alzheimer's disease *via* the STAT2−SIRT4−mTOR pathway. *Am J Physiol Cell Physiol* 2024; **326**:C1697−709.
63. Okamoto N, Sato Y, Kawagoe Y, Shimizu T, Kawamura K. Short-term resveratrol treatment restored the quality of oocytes in aging mice. *Aging (Albany NY)* 2022;**14**:5628−40.
64. Zeng J, Jiang M, Wu X, Diao F, Qiu D, Hou X, et al. SIRT4 is essential for metabolic control and meiotic structure during mouse oocyte maturation. *Aging Cell* 2018;**17**:e12789.
65. Fu L, Dong Q, He J, Wang X, Xing J, Wang E, et al. SIRT4 inhibits malignancy progression of NSCLCs, through mitochondrial dynamics mediated by the ERK−Drp1 pathway. *Oncogene* 2017;**36**: 2724−36.